ARTICLE

doi:10.1038/nature17624

Distinct bone marrow blood vessels differentially regulate haematopoiesis

Tomer Itkin[1], Shiri Gur-Cohen[1], Joel A. Spencer[2,3], Amir Schajnovitz[4,5,6], Saravana K. Ramasamy[7], Anjali P. Kusumbe[7], Guy Ledergor[1,8], Yookyung Jung[2,3], Idan Milo[1], Michael G. Poulos[9], Alexander Kalinkovich[1], Aya Ludin[1], Karin Golan[1], Eman Khatib[1], Anju Kumari[1], Orit Kollet[1], Guy Shakhar[1], Jason M. Butler[9], Shahin Rafii[9], Ralf H. Adams[7], David T. Scadden[4,5,6], Charles P. Lin[2,3] & Tsvee Lapidot[1]

Bone marrow endothelial cells (BMECs) form a network of blood vessels that regulate both leukocyte trafficking and haematopoietic stem and progenitor cell (HSPC) maintenance. However, it is not clear how BMECs balance these dual roles, and whether these events occur at the same vascular site. We found that mammalian bone marrow stem cell maintenance and leukocyte trafficking are regulated by distinct blood vessel types with different permeability properties. Less permeable arterial blood vessels maintain haematopoietic stem cells in a low reactive oxygen species (ROS) state, whereas the more permeable sinusoids promote HSPC activation and are the exclusive site for immature and mature leukocyte trafficking to and from the bone marrow. A functional consequence of high permeability of blood vessels is that exposure to blood plasma increases bone marrow HSPC ROS levels, augmenting their migration and differentiation, while compromising their long-term repopulation and survival. These findings may have relevance for clinical haematopoietic stem cell transplantation and mobilization protocols.

Vascular-forming endothelial cells form a vast network which participates in homeostasis and metabolism regulation, delivering oxygen, nutrients and other building blocks to distinct organs. This diverse network also serves as a cellular highway allowing trafficking of blood cells, leukocytes and other cell types throughout the body. In addition, endothelial cells serve an important role as regulators of organ homeostasis and regeneration via direct interactions with local stem and progenitor cells, and by secretion of angiocrine factors[1]. BMECs form a mechanical barrier, which prevents entry into the bone marrow of mature red blood cells and platelets from the circulation, regulating cellular trafficking, haematopoiesis and osteogenesis[2–4]. BMECs also contribute to specialized perivascular microenvironments where the majority of bone marrow haematopoietic stem and progenitor cells (HSPCs) reside[5–8]. BMEC perivascular domains include heterogeneous populations of mesenchymal stromal precursor cells (MSPCs) previously reported to regulate HSPCs[9–11]. In addition, BMECs provide angiocrine signals that regulate haematopoietic stem cell development and haematopoiesis[10,12,13]. Different types of blood vessels compose the bone marrow vascular network[4,11,12], exhibiting distinct properties and forming unique domains. We investigated how BMECs exert their dual roles as regulators of stem cell maintenance and of cellular trafficking, and if these distinct roles are associated with specialized blood vessels sub-types and specific micro-anatomical regions. We characterized the bone marrow vascular architecture, the properties of the distinct types of blood vessels, and their associated 'niche' cells participating in the formation of unique bone marrow multi-cellular domains. Finally, whether manipulation of endothelial properties may serve to control tissue homeostasis and stem cell fate was examined.

Defining bone marrow vascular architecture and domains

We used Sca-1–EGFP (Sca-1, also known as Ly6a) transgenic mice to distinguish between Sca-1$^-$ sinusoidal BMECs (sBMECs) from Sca-1$^+$ arterial BMECs (aBMECs)[12]. Arterial BMECs (23.5 ± 3.1% of BMECs, Fig. 1a) display unique elongated elliptical nuclear morphology (Fig. 1b, f). Adherence and tight junction molecules VE-cadherin and ZO-1 were highly and preferentially expressed by aBMECs (Fig. 1c and Extended Data Fig. 1a). Sca-1$^+$ blood vessels had smaller diameters compared to neighbouring Sca-1$^-$ sinusoids, and were closely associated with calcified bone at the metaphysis or in the diaphysis (Fig. 1d and Supplementary Video 1). Arteries co-stained for Sca-1 and CD31, and were enwrapped by αSMA$^+$ pericytes (Fig. 1e). Approaching the endosteum, arteries branched into smaller arterioles that were not associated with αSMA$^+$ pericytes, but were instead surrounded by Sca-1$^+$ mesenchymal (reticular) and clusters of Sca-1$^+$ haematopoietic (round) cells (Fig. 1e). Combining osteopontin (OPN) staining for bone-lining osteoblasts with endothelial markers (Extended Data Fig. 1b), revealed that the vast majority of arterial blood vessels are found at a distance of <40 μm from the endosteum, with ~50% at a closer distance of <20 μm from the endosteum (Extended Data Fig. 1c). Arteries enwrapped by αSMA$^+$ pericytes had an approximately 10 μm diameter, branching to smaller ~5 μm diameter endosteal arterioles, connecting downstream to much larger ~25 μm sinusoids (Extended Data Fig. 1d).

High intracellular levels of reactive oxygen species (ROS) hamper bone marrow haematopoietic stem cell quiescence, accelerating their differentiation and exhaustion[14,15]. Elevated ROS levels also promote HSPC mobilization by activating their motility machinery[16,17]. Detecting intracellular ROS^{high} expressing cells (Extended Data Fig. 1e, f), we found there were lower frequencies of ROS^{high} cells adjacent to arteries (Fig. 1f (top and middle) and Extended Data Fig. 1g), compared to sinusoids (Fig. 1f (bottom) and Extended Data Fig. 1g). SLAM HSPCs associated with sinusoids and positioned >20 μm from aBMECs (41 out of 41), had either negative or low (26 out of 41) or high (15 out of 41) ROS levels (Extended Data Fig. 1h, i). In contrast, SLAM HSPCs associated with arteries were consistently

[1]Department of Immunology, The Weizmann Institute of Science, Rehovot 76100, Israel. [2]Wellman Center for Photomedicine, Massachusetts General Hospital, Harvard Medical School, Boston, Massachusetts 02114, USA. [3]Center for Systems Biology, Massachusetts General Hospital, Harvard Medical School, Boston, Massachusetts 02114, USA. [4]Department of Stem Cell and Regenerative Biology, Harvard University, Cambridge, Massachusetts 02138, USA. [5]Harvard Stem Cell Institute, Cambridge, Massachusetts 02114, USA. [6]Center for Regenerative Medicine and Cancer Center, Massachusetts General Hospital, Boston, Massachusetts 02114, USA. [7]Max Planck Institute for Molecular Biomedicine, Department of Tissue Morphogenesis and Faculty of Medicine, University of Münster, D-48149 Münster, Germany. [8]Internal Medicine Department, Tel-Aviv Sourasky Medical Center, Tel-Aviv 64239, Israel. [9]Department of Genetic Medicine, Weill Cornell Medical College, New York, New York 10065, USA.

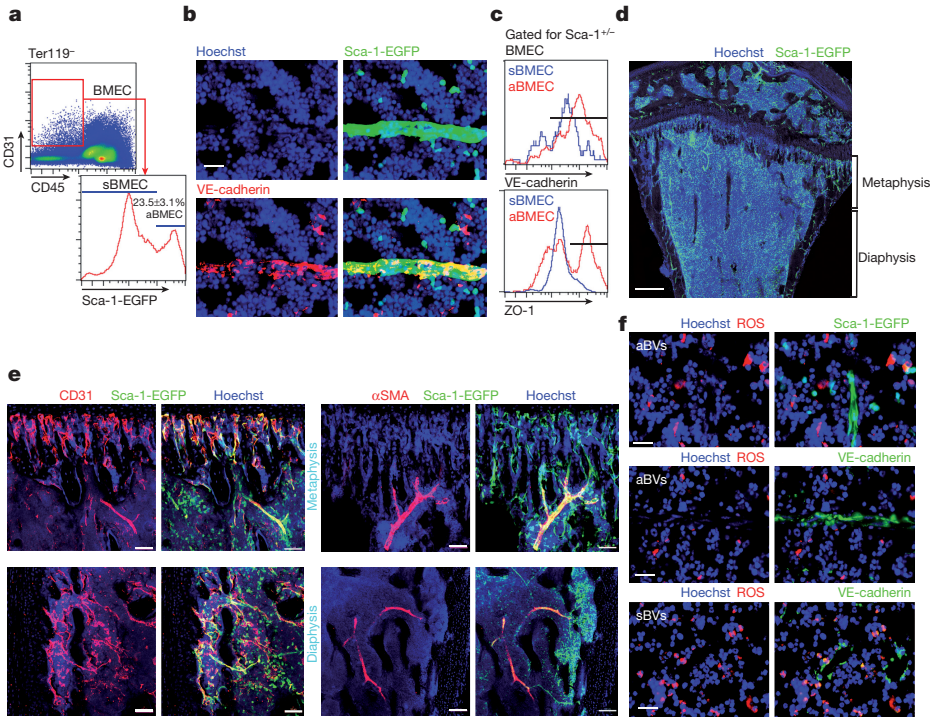

Figure 1 | Sca-1 and nestin distinguish less permeable arterial bone marrow blood vessels, which sustain ROS^{low} HSC. a, Representative flow cytometry density and histogram plots for BMECs (mean ± s.e.m., $n = 6$ mice from three independent experiments). **b**, Representative fluorescence images of a small diameter blood vessel from the metaphysial area expressing Sca-1-EGFP (green), junctional VE-cadherin (red) and elongated nuclei (Hoechst, blue). Scale bar indicates 20 μm. **c**, VE-cadherin and ZO-1 flow cytometry representative histogram plots for mean fluorescent intensity expression (MFI) by BMECs. ($n = 9$ mice from three independent experiments). **d**, Representative confocal tile scan of Sca-1-EGFP (green) femur. Scale bar indicates 300 μm. **e**, Representative confocal images of endosteal regions in the metaphysis and diaphysis showing Sca-1$^+$ (green)/CD31$^+$ (red) arterial blood vessels and αSMA$^+$ (red) pericytes. Scale bars in panels indicate 50 μm, except for the lower right panels where scale bar indicates 100 μm. **f**, Representative fluorescence images of ROS^{high} (red) expressing cells in the proximate microenvironment of Sca-1$^+$ (green) or VE-cadherin$^+$ (green) arterioles (top and middle panels, respectively) and VE-cadherin$^+$ (green) sinusoids (bottom panels). Scale bar indicates 20 μm.

negative for ROS staining (22 out of 22) (Extended Data Fig. 1j). The ROS^{low} SLAM HSPCs distant from arteries, resided in close proximity to megakaryocytes (<20 μm) consistent with the quiescent megakaryocytic stem cell niche reports[18–20] (Extended Data Fig. 1h). Our data indicate that HSPCs spatial bone marrow localization is dependent on HSPC metabolic state. However, in agreement with a recent study[21], we confirmed that, if their metabolic state is ignored, SLAM HSPCs had random localization among distinct bone marrow regions (Extended Data Fig. 1k).

BMECs and neighbouring MSPCs characterization

As specific sub-types of endosteal blood vessels serve as regulatory niches for bone-forming mesenchymal stromal precursor cells (MSPCs)[4], we analysed blood vessels for expression of the pericyte and MSPC marker NG2 (also known as CSPG4 in humans) and nestin[9,11,13]. NG2 stained a heterogeneous population, negative and positive for Sca-1, enwrapping Sca-1$^+$ blood vessels (Extended Data Fig. 2a). Unexpectedly, Sca-1 staining on bone marrow sections from mice with a nestin promoter driving GFP expression (nestin-GFP), reported to label HSC-supportive bone marrow MSPCs[9], revealed the existence of nestin$^+$ BMECs with elongated nuclei expressing Sca-1 and VE-cadherin (Extended Data Fig. 2b, c). Nestin$^+$ precursor cells give rise to both endothelial and mesenchymal lineages[22], and we have occasionally detected very bright nestin$^+$Sca-1$^-$ MSPCs[11] adjacent to nestin$^+$Sca-1$^+$ BMECs (Extended Data Fig. 2b). Nestin$^+$NG2$^+$ MSPCs were tightly associated with nestin$^+$NG2$^-$ blood vessels (Extended Data Fig. 2d). Nestin$^+$ blood vessels are mostly small diameter, di-acetyl low-density lipoprotein (LDL)-negative blood vessels, associated with calcified bone (Extended Data Fig. 2e and Supplementary Video 2). Among CD45$^-$CD31$^+$ BMECs, nestin expression was restricted to Sca-1$^+$CD31^{high} aBMECs, and was absent from Sca-1$^-$CD31$^+$ sBMECs (Extended Data Fig. 2f, g). Nestin-GFP was also expressed by heterogeneous populations of mesenchymal[9] and haematopoietic[23] populations (Extended Data Fig. 2g). Nestin$^+$ blood vessels and MSPCs were predominantly detected at the metaphysis and adjacent to cortical bone at the diaphysis (Extended Data Fig. 2h, i). Nestin expressing non-myelinating Schwann cells that maintain hibernating HSC[24], were exclusively associated only with arteries, contributing to metabolically 'low' microenvironments (Extended Data Fig. 2j–l).

Further profiling expression of endothelial molecules involved in leukocyte trafficking, revealed that aBMECs express higher levels of VCAM-1, ICAM-1, P-selectin and preferentially expressed JAM-A, whereas sBMECs preferentially express higher levels of E-selectin (Extended Data Fig. 3a–f), which is involved in HSPCs bone marrow homing[6]. In addition to their role in leukocyte trafficking, these adhesion molecules also control HSPC retention by VCAM-1 (ref. 25) or negative regulation of HSC quiescence by E-selectin[26]. Endothelial metabolism, more specifically glycolysis rather than oxidative phosphorylation, regulates vessel development and function[27,28]. We noted that aBMEC exhibit lower ROS levels and higher glucose uptake relative to sBMEC (Extended Data Fig. 3g, h). This finding may indicate that aBMECs represent a more actively developing sub-type of BMEC and correlates with the observation that bone marrow oxygen tension is highest near and in arterial BVs[29] skewing arteries to the glycolytic pathway to avoid excessive ROS production[28].

Sinusoids are the exclusive trafficking sites

Relatively to sinusoids, the preceding arterial nestin$^+$ blood vessels displayed lower permeability and dramatically higher blood flow and

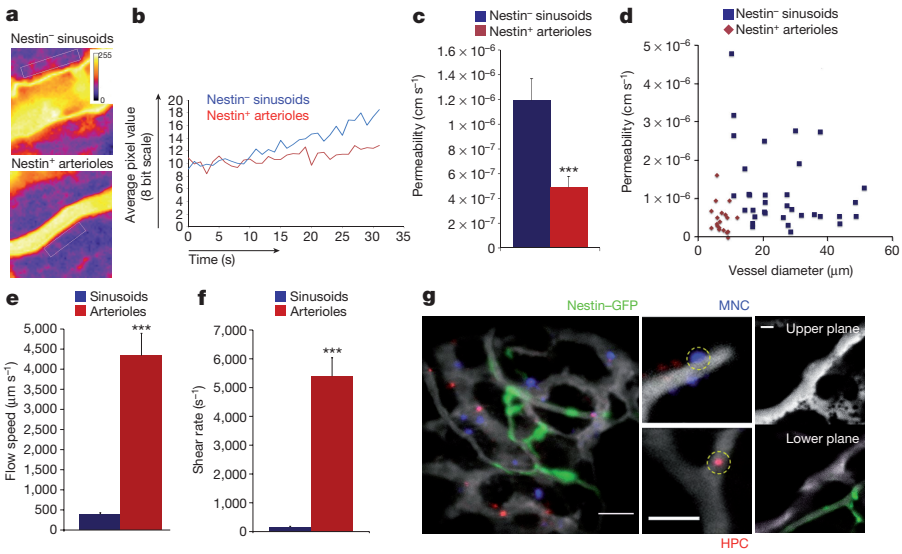

Figure 2 | Leaky sinusoids are the exclusive site for cellular trafficking. **a**, Standard deviation heat map of rhodamine–dextran leakage. Colour scale shows pixel intensity over 30 s of data acquisition. Regions of interest are bordered with a white line. **b**, Time traces of fluorescence signal. **c**, Average vascular permeability. **d**, A plot of permeability measurements as a function of vessel diameter. **e**, **f**, Average blood flow speed and shear rate. **g**, Representative maximum intensity images demonstrating homing of adoptively transferred lineage depleted HPC (haematopoietic progenitor cells, red) and bone marrow mononuclear cells (MNC) (blue) within the bone marrow of a nestin-GFP (green) mouse (left); transmigrating bone marrow MNC (circled, blue) and adherent Lin$^-$ HPC (circled, red), scale bar indicates 50 μm (middle); upper and lower planes of the *z*-stack taken from Supplementary Video 9 representing the relative proximity of a nestin$^+$ blood vessel to a sinusoidal trafficking site (right), scale bar indicates 25 μm, $n = 309$ trafficking events were monitored and analysed. **a**–**g**, Mean ± s.e.m., $n = 53$ blood vessels were analysed for permeability measurements and $n = 62$ blood vessels were analysed for blood flow/shear rates, from three independent experiments each). Two-tailed Student's *t*-test; $^{***}P < 0.005$.

shear rates (Fig. 2a–f and Supplementary Videos 3–5). Comparing calvarial to femoral (including both diaphysis and metaphysis regions) bones, no major differences were noted in blood vessel distribution, blood vessel size, sinusoidal blood vessel properties or permeability, but the calvarial bone contained a higher frequency of BMECs, including a higher frequency of aBMEC, displaying characteristics of enhanced integrity (Extended Data Fig. 4a–e).

Phenotypically defined long-term repopulating (LTR)-HSCs are reported to localize preferentially near nestin$^+$ stromal cells[9]. The lower permeability, the high-flow speed[29], and high shear rates in arterial nestin$^+$ blood vessels suggest that a different type of blood vessel serves as a site for HSPCs and mature leukocyte trafficking and homing to the bone marrow. We observed that haematopoietic cell rolling and adhesion events occurred exclusively in sinusoids (377 out of 377

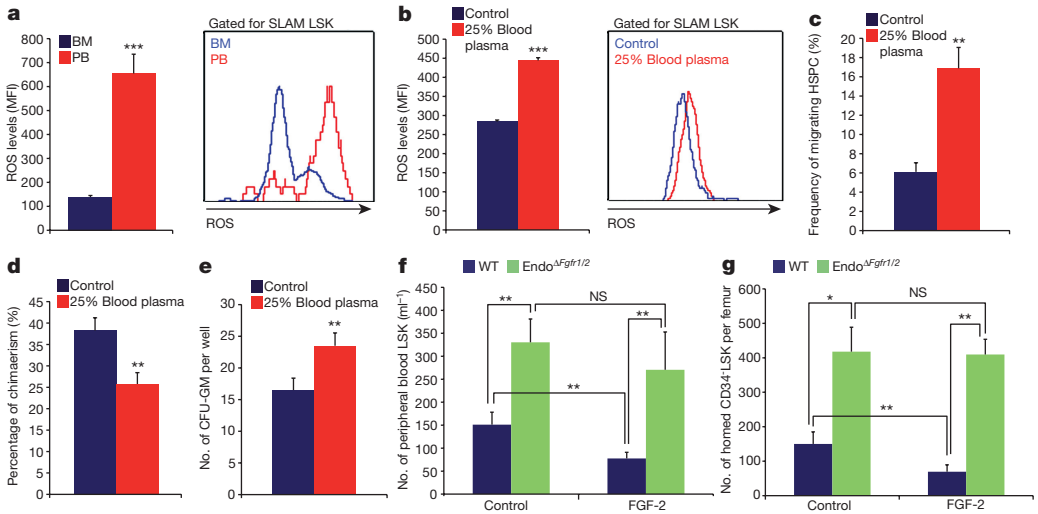

Figure 3 | Plasma penetration through leaky endothelium dictates HSPC trafficking and development. **a**, HSPCs ROS MFI quantitative analysis and representative histogram plot. Mean ± s.e.m., $n = 6$ mice from three independent experiments. Two-tailed Student's *t*-test, $^{***}P < 0.005$. **b**–**e**, Bone marrow cells were incubated for 2 h with (25% blood plasma) or without (control) peripheral blood plasma. Mean ± s.e.m., $n = 9$ repeats in triplicates from three independent experiments. Two-tailed Student's *t*-test; $^{**}P < 0.01$, $^{***}P < 0.005$. **b**, HSPCs ROS MFI quantitative analysis and representative histogram plot. **c**, HSPC migration frequency. **d**, Chimaerism levels indicating LTR-HSC contribution. Mean ± s.e.m., $n = 27$ donor from three independent experiments, with at least 3 recipient mice per donor. **e**, Average number of colony-forming units granulocytes/macrophages (CFU-GM) . **f**, Numbers of LSK HSPCs in the blood. Mean ± s.e.m., $n = 9$ mice from three independent experiments. Two-way ANOVA with Bonferroni's multiple comparison post-hoc test; $^{**}P < 0.01$. **g**, HSPC homing per femur. Mean ± s.e.m., $n = 5$ mice from 2 independent experiments. Two-way ANOVA with Bonferroni's multiple comparison post-hoc test; $^{*}P < 0.05$, $^{**}P < 0.01$.

events, Supplementary Video 6 and Extended Data Fig. 4f, g). Similarly, transendothelial migration of mature leukocytes and immature HSPCs occurred exclusively via sinusoids (observed in 309 out of 309 events, Fig. 2g and Supplementary Videos 7–10).

Endothelial CXCL12 and CXCR4 in HSC mobilization

AMD3100 treatment, an agent that induces rapid HSPC mobilization[30] via shedding and release of chemoattractant cytokines, such as stem cell factor (SCF) and CXCL12, from bone marrow cells into the blood[31,32], reduced vascular integrity and cytokine abundance, preferentially on sBMECs (Extended Data Fig. 5a–d). Furthermore, AMD3100 led to reduced CXCR4 phosphorylation by BMEC, 5 min after treatment (Extended Data Fig. 5e). CXCR4 neutralization treatment increased vascular permeability as well (Extended Data Fig. 5f). However, since these antibodies also directly inhibit HSPC egress and mobilization[32], *Cxcr4* was specifically deleted in endothelial cells (Endo$^{\Delta Cxcr4}$, Extended Data Fig. 5g–j). Increased vascular permeability and enhanced HSPC egress were observed in Endo$^{\Delta Cxcr4}$ mice (Extended Data Fig. 5k–m). Supported by previous *in vitro* findings[33], our data indicate that CXCR4 signalling regulates bone marrow vascular integrity and, as a consequence, HSPC trafficking.

A leaky endothelium promotes HSPC trafficking

To delineate a potential connection between blood vessel permeability allowing penetration of blood plasma into the bone marrow and HSC development, bone-marrow-residing SLAM LSK HSPCs were compared with circulating SLAM LSK HSPCs in the peripheral blood. ROS levels in peripheral blood circulating HSPCs were much higher relative to bone-marrow-residing HSPCs (Fig. 3a). Short *in vitro* exposure of bone marrow HSPCs to peripheral blood plasma augmented intracellular ROS levels, resulting in their enhanced migratory capacity (Fig. 3b, c). Yet it also enhanced the frequency of apoptotic HSPCs, slightly increased HSPC cycling, along with enhanced differentiation, leading to reduced LTR-HSC capacity (Fig. 3d, e and Extended Data Fig. 6a, b).

We tested whether the state of endothelial integrity affects bone marrow HSC fate. Fibroblast growth factor (FGF) signalling has important roles in long-term repopulating HSCs (LTR-HSCs) maintenance and expansion[34,35] and in maintaining endothelial integrity[36,37]. Consistent with this, induction of FGF signalling enhanced bone marrow endothelial barrier integrity (Extended Data Fig. 6c–e). In addition, it led to significant changes in bone marrow vascular architecture (Extended Data Fig. 6f–j). As a consequence, HSPCs and MSPCs fates were affected, resulting in their expansion[34], reduced HSPCs and LTR-HSCs bi-directional trafficking, reduced MSPC differentiation and a shift in HSPC metabolism (Extended Data Fig. 6k–q).

To segregate endothelial mediated effects, FGFR1 and FGFR2 were deleted specifically in endothelial cells (Endo$^{\Delta Fgfr1/2}$) (Extended Data Fig. 5g). Impairment in endothelial integrity (Extended Data Fig. 7a–c) was measured in Endo$^{\Delta Fgfr1/2}$ mice. Consistent with their impaired

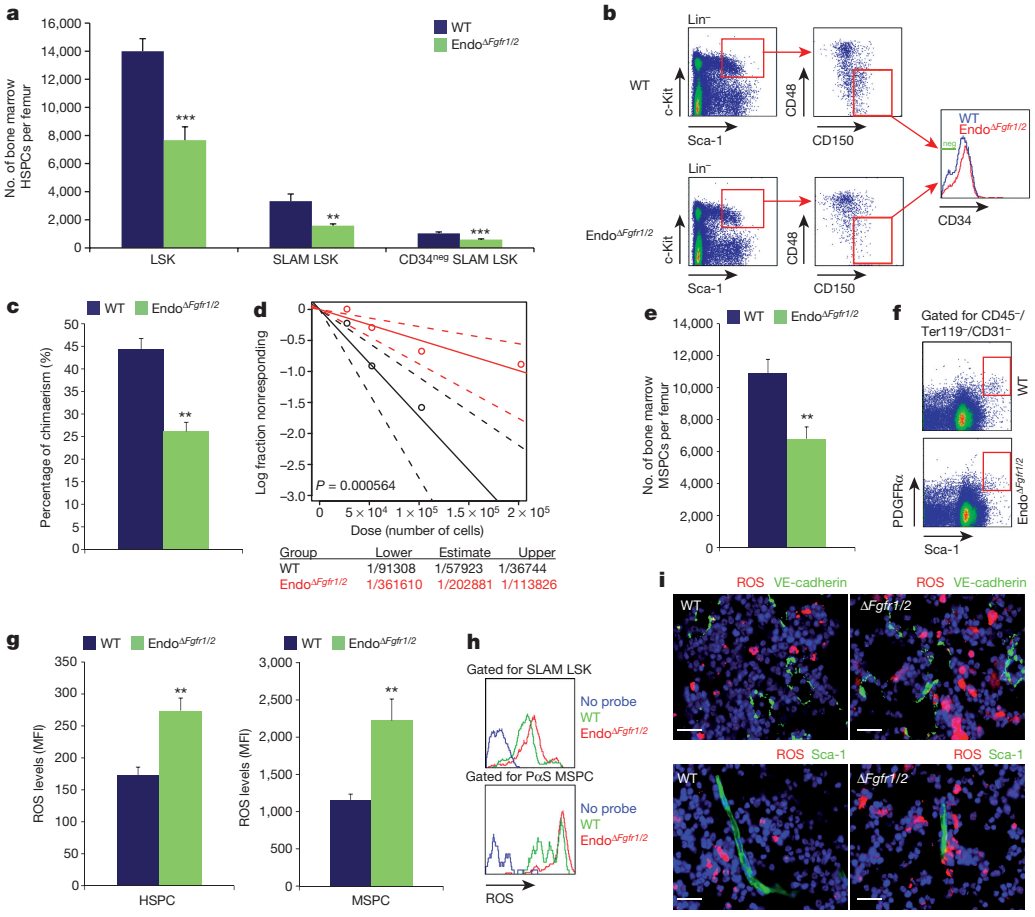

Figure 4 | Reducing endothelial barrier integrity hampers stem cell maintenance. a, **b**, Quantitative analysis and representative plots of HSPC populations. **c**, Chimaerism levels indicating LTR-HSC contribution. Mean ± s.e.m., $n = 18$ donor mice from two independent experiments, with 3 recipient mice per donor. **d**, Repopulating units frequency in the bone marrow indicating HSC numbers ($n = 60$ donor mice from 2 independent experiments, for 3 recipient mice per dilution per donor). **e**, **f**, Quantitative analysis and representative density plots of MSPCs. **g**, **h**, Quantitative analysis and representative histogram plots of HSPCs and PαS MSPCs ROS MFIs. **i**, Representative images of ROS^{high} (red) cells in proximity to blood vessels. Scale bar indicates 20 μm. **a**–**h**, Mean ± s.e.m., $n = 9$ mice from three independent experiments. Two-tailed Student's *t*-test; $^{**}P < 0.01$, $^{***}P < 0.005$.

barrier status, Endo$^{\Delta Fgfr1/2}$ mice demonstrated increased HSPC bi-directional trafficking (Fig. 3f, g). In contrast to wild-type (WT) mice, FGF-2 treatment of Endo$^{\Delta Fgfr1/2}$ mice failed to reduce or prevent this phenomenon (Fig. 3f, g). Also, this model of endothelial FGF loss-of-function displayed notable changes in bone marrow vascular architecture and properties (Extended Data Fig. 7d–j).

Vascular integrity maintains bone marrow stem cells

We next investigated bone marrow HSC maintenance under conditions of impaired endothelial integrity. Endothelial barrier disruption in of Endo$^{\Delta Fgfr1/2}$ mice led to a significant reduction in the numbers of HSPCs/LTR-HSCs and bone marrow PDFGRα^{+}Sca-1^{+} (PαS) MSPCs[38] (Fig. 4a–f). Both HSPCs and MSPCs displayed increased ROS levels (Fig. 4g, h), and the frequency of ROS^{high} cells surrounding blood vessels was increased (Fig. 4i and Extended Data Fig. 7k).

Along with elevation in ROS levels, glucose uptake was enhanced by both HSPCs and MSPCs (Extended Data Fig. 7m and 8a) in Endo$^{\Delta Fgfr1/2}$ mice, indicating an augmentation of the oxidative phosphorylation pathway in these populations. Similar to plasma-exposed bone marrow HSPCs, HSPCs derived from Endo$^{\Delta Fgfr1/2}$ mice bone marrow exhibited a slight elevation in cycling state, a striking increase in apoptosis, and following transplantation, a differentiation skewing towards the myeloid lineage (Extended Data Fig. 7n–q). The functional role of elevated ROS levels in HSPCs from Endo$^{\Delta Fgfr1/2}$ mice was tested using the ROS scavenger *N*-acetyl-L-cysteine (NAC). Prolonged NAC treatment restored normal levels of HSPC egress to the peripheral blood, and normal levels of bone marrow HSPC and LTR-HSC in Endo$^{\Delta Fgfr1/2}$ mice (Extended Data Fig. 7r–t).

As MSPC metabolism and glucose uptake regulate bone formation[39], and plasma-borne factors such as vitamin E can penetrate the bone marrow and influence bone remodelling[40], stromal development was examined under conditions of a hampered endothelial bone marrow barrier. Accelerated stromal differentiation at the expense of the MSPC pool was observed (Extended Data Fig. 8a–d) alongside with dramatic changes in the bone marrow concentrations of the hormones calcitonin and parathyroid hormone (PTH), regulating bone formation and remodelling, responding to changes in endothelial integrity (Extended Data Fig. 8j–m).

We also applied a pharmacological model to disrupt endothelial integrity by infusing neutralizing anti-VE-cadherin antibodies (Extended Data Fig. 9a). This model mimicked our genetic model affecting HSPC bi-directional trafficking and LTR-HSC maintenance which were also ROS dependent (Extended Data Fig. 9b–k). Vascular architecture and stromal development were also severely altered in this model of barrier manipulation (Extended Data Figs 7l, 8e–i, and 9l–q).

Discussion

In this study, the roles of BMECs as regulators of haematopoiesis were investigated. The existence of diverse vascular niches was investigated and an endosteal-vascular niche is supported by data showing that less permeable endosteal blood vessels provide a microenvironment promoting ROS^{low} HSC maintenance (summarized in Extended Data Fig. 10). In support of this, specialized aPC-secreting bone marrow arteries retain EPCR^{+} LTR-HSC via downregulation of nitric oxide production, enhancing adhesion and reducing migration[41]. These data sets add new information to previous reports that BrdU-retaining HSCs are mostly localized in endosteal regions[42], where HSCs are maintained in a quiescent mode[43,44]. We extended previous studies reporting similar niches at steady-state[21] and in irradiated transplanted recipient mice[8,45], located mainly at trabecular regions between the endosteal surface and previously undefined blood vessels. Notably, an HSPC sub-population expressing α-catulin, which is also expressed by activated migrating endothelial cells[46], preferentially localized to bone marrow perisinusoidal domains[47]. We show that many cell types which participate in and form the bone marrow HSC niches, share overlapping cell surface markers, including different endothelial, mesenchymal, haematopoietic and neuronal cells. We reveal for the first time (to our knowledge), distinct sinusoidal sites for leukocyte trafficking, where entry and exit from the circulation occurs and metabolic parameters such as ROS are regulated (summarized in Extended Data Fig. 10). ROS augmentation at these sites is manifested by penetrating plasma, via fenestrated endothelium, probably carrying HSC ROS-inducing factors, found in higher concentration in the blood[17]. Our results suggest that prolonged HSC loitering in the peripheral blood might be hazardous for their stemness properties and should be taken into account for clinical mobilization protocols. This is similar to cases of extraphysiologically driven oxygen shock which elevates ROS levels, reducing LTR-HSC capacity in favour of more committed, maturing progenitors[48]. Endothelial cells are exposed to the highest levels of physiological oxygen tension and therefore have developed internal mechanisms to scavenge excessive ROS molecules and rely mainly on glycolysis to avoid ROS production via oxidative phosphorylation[28]. ROS levels were not altered in BMECs in all the manipulation models (data not shown); however, NAC-mediated rescue of the HSC phenotype was confirmed. Prolonged NAC treatment reduced HSPC egress to the peripheral blood; however, it had no effect on endothelial barrier integrity (Extended Data Fig. 9r–t). These results reveal how NAC pre-treatment increases transplanted HSC bone marrow engraftment[49,50], as it has no effect on barrier permeability, allowing successful HSPC bone marrow homing, and it may also promote a ROS-low supportive stem cell retaining microenvironment. The dynamic and versatile endothelial barrier may enable new approaches to control stem cell functions relevant for clinical stem cell mobilization and transplantation protocols to enhance HSPCs egress to the peripheral blood, to promote successful bone marrow lodgment of transplanted HSCs, and to expand engrafting HSCs following transplantation, by restricting or permitting the degree of plasma penetration.

Online Content Methods, along with any additional Extended Data display items and Source Data, are available in the online version of the paper; references unique to these sections appear only in the online paper.

Received 13 January 2015; accepted 25 February 2016.
Published online 13 April 2016.

1. Rafii, S., Butler, J. M. & Ding, B. S. Angiocrine functions of organ-specific endothelial cells. *Nature* **529,** 316–325 (2016).
2. Lapidot, T., Dar, A. & Kollet, O. How do stem cells find their way home? *Blood* **106,** 1901–1910 (2005).
3. Morrison, S. J. & Scadden, D. T. The bone marrow niche for haematopoietic stem cells. *Nature* **505,** 327–334 (2014).
4. Kusumbe, A. P., Ramasamy, S. K. & Adams, R. H. Coupling of angiogenesis and osteogenesis by a specific vessel subtype in bone. *Nature* **507,** 323–328 (2014).
5. Kiel, M. J., Yilmaz, O. H., Iwashita, T., Terhorst, C. & Morrison, S. J. SLAM family receptors distinguish hematopoietic stem and progenitor cells and reveal endothelial niches for stem cells. *Cell* **121,** 1109–1121 (2005).
6. Sipkins, D. A. *et al. In vivo* imaging of specialized bone marrow endothelial microdomains for tumour engraftment. *Nature* **435,** 969–973 (2005).
7. Colmone, A. *et al.* Leukemic cells create bone marrow niches that disrupt the behavior of normal hematopoietic progenitor cells. *Science* **322,** 1861–1865 (2008).
8. Lo Celso, C. *et al.* Live-animal tracking of individual haematopoietic stem/progenitor cells in their niche. *Nature* **457,** 92–96 (2009).
9. Méndez-Ferrer, S. *et al.* Mesenchymal and haematopoietic stem cells form a unique bone marrow niche. *Nature* **466,** 829–834 (2010).
10. Ding, L., Saunders, T. L., Enikolopov, G. & Morrison, S. J. Endothelial and perivascular cells maintain haematopoietic stem cells. *Nature* **481,** 457–462 (2012).
11. Kunisaki, Y. *et al.* Arteriolar niches maintain haematopoietic stem cell quiescence. *Nature* **502,** 637–643 (2013).
12. Hooper, A. T. *et al.* Engraftment and reconstitution of hematopoiesis is dependent on VEGFR2-mediated regeneration of sinusoidal endothelial cells. *Cell Stem Cell* **4,** 263–274 (2009).
13. Isern, J. *et al.* The neural crest is a source of mesenchymal stem cells with specialized hematopoietic stem cell niche function. *Elife* **3,** e03696 (2014).
14. Ito, K. *et al.* Reactive oxygen species act through p38 MAPK to limit the lifespan of hematopoietic stem cells. *Nature Med.* **12,** 446–451 (2006).
15. Miyamoto, K. *et al.* Foxo3a is essential for maintenance of the hematopoietic stem cell pool. *Cell Stem Cell* **1,** 101–112 (2007).
16. Tesio, M. *et al.* Enhanced c-Met activity promotes G-CSF-induced mobilization of hematopoietic progenitor cells via ROS signaling. *Blood* **117,** 419–428 (2011).

17. Golan, K. *et al.* S1P promotes murine progenitor cell egress and mobilization via S1P1-mediated ROS signaling and SDF-1 release. *Blood* **119,** 2478–2488 (2012).
18. Zhao, M. *et al.* Megakaryocytes maintain homeostatic quiescence and promote post-injury regeneration of hematopoietic stem cells. *Nature Med.* **20,** 1321–1326 (2014).
19. Bruns, I. *et al.* Megakaryocytes regulate hematopoietic stem cell quiescence through CXCL4 secretion. *Nature Med.* **20,** 1315–1320 (2014).
20. Nakamura-Ishizu, A., Takubo, K., Fujioka, M. & Suda, T. Megakaryocytes are essential for HSC quiescence through the production of thrombopoietin. *Biochem. Biophys. Res. Commun.* **454,** 353–357 (2014).
21. Nombela-Arrieta, C. *et al.* Quantitative imaging of haematopoietic stem and progenitor cell localization and hypoxic status in the bone marrow microenvironment. *Nature Cell Biol.* **15,** 533–543 (2013).
22. Ono, N. *et al.* Vasculature-associated cells expressing nestin in developing bones encompass early cells in the osteoblast and endothelial lineage. *Dev. Cell* **29,** 330–339 (2014).
23. Ludin, A. *et al.* Monocytes-macrophages that express α-smooth muscle actin preserve primitive hematopoietic cells in the bone marrow. *Nature Immunol.* **13,** 1072–1082 (2012).
24. Yamazaki, S. *et al.* Nonmyelinating Schwann cells maintain hematopoietic stem cell hibernation in the bone marrow niche. *Cell* **147,** 1146–1158 (2011).
25. Papayannopoulou, T., Priestley, G. V., Nakamoto, B., Zafiropoulos, V. & Scott, L. M. Molecular pathways in bone marrow homing: dominant role of $\alpha_4\beta_1$ over β_2-integrins and selectins. *Blood* **98,** 2403–2411 (2001).
26. Winkler, I. G. *et al.* Vascular niche E-selectin regulates hematopoietic stem cell dormancy, self renewal and chemoresistance. *Nature Med.* **18,** 1651–1657 (2012).
27. De Bock, K. *et al.* Role of PFKFB3-driven glycolysis in vessel sprouting. *Cell* **154,** 651–663 (2013).
28. Vandekeere, S., Dewerchin, M. & Carmeliet, P. Angiogenesis revisited: an overlooked role of endothelial cell metabolism in vessel sprouting. *Microcirculation* **22,** 509–517 (2015).
29. Spencer, J. A. *et al.* Direct measurement of local oxygen concentration in the bone marrow of live animals. *Nature* **508,** 269–273 (2014).
30. Broxmeyer, H. E. *et al.* Rapid mobilization of murine and human hematopoietic stem and progenitor cells with AMD3100, a CXCR4 antagonist. *J. Exp. Med.* **201,** 1307–1318 (2005).
31. Heissig, B. *et al.* Recruitment of stem and progenitor cells from the bone marrow niche requires MMP-9 mediated release of Kit-ligand. *Cell* **109,** 625–637 (2002).
32. Dar, A. *et al.* Rapid mobilization of hematopoietic progenitors by AMD3100 and catecholamines is mediated by CXCR4-dependent SDF-1 release from bone marrow stromal cells. *Leukemia* **25,** 1286–1296 (2011).
33. Kobayashi, K. *et al.* Stromal cell-derived factor-1α/C-X-C chemokine receptor type 4 axis promotes endothelial cell barrier integrity via phosphoinositide 3-kinase and Rac1 activation. *Arterioscler. Thromb. Vasc. Biol.* **34,** 1716–1722 (2014).
34. Itkin, T. *et al.* FGF-2 expands murine hematopoietic stem and progenitor cells via proliferation of stromal cells, c-Kit activation, and CXCL12 down-regulation. *Blood* **120,** 1843–1855 (2012).
35. Zhao, M. *et al.* FGF signaling facilitates postinjury recovery of mouse hematopoietic system. *Blood* **120,** 1831–1842 (2012).
36. Murakami, M. *et al.* The FGF system has a key role in regulating vascular integrity. *J. Clin. Invest.* **118,** 3355–3366 (2008).
37. De Smet, F. *et al.* Fibroblast growth factor signaling affects vascular outgrowth and is required for the maintenance of blood vessel integrity. *Chem. Biol.* **21,** 1310–1317 (2014).
38. Houlihan, D. D. *et al.* Isolation of mouse mesenchymal stem cells on the basis of expression of Sca-1 and PDGFR-α. *Nature Protocols* **7,** 2103–2111 (2012).
39. Wei, J. *et al.* Glucose uptake and Runx2 synergize to orchestrate osteoblast differentiation and bone formation. *Cell* **161,** 1576–1591 (2015).
40. Fujita, K. *et al.* Vitamin E decreases bone mass by stimulating osteoclast fusion. *Nature Med.* **18,** 589–594 (2012).
41. Gur-Cohen, S. *et al.* PAR1 signaling regulates the retention and recruitment of EPCR-expressing bone marrow hematopoietic stem cells. *Nature Med.* **21,** 1307–1317 (2015).
42. Zhang, J. *et al.* Identification of the haematopoietic stem cell niche and control of the niche size. *Nature* **425,** 836–841 (2003).
43. Arai, F. *et al.* Tie2/angiopoietin-1 signaling regulates hematopoietic stem cell quiescence in the bone marrow niche. *Cell* **118,** 149–161 (2004).
44. Sugimura, R. *et al.* Noncanonical Wnt signaling maintains hematopoietic stem cells in the niche. *Cell* **150,** 351–365 (2012).
45. Xie, Y. *et al.* Detection of functional haematopoietic stem cell niche using real-time imaging. *Nature* **457,** 97–101 (2009).
46. Bear, M. D. *et al.* Alpha-Catulin co-localizes with vimentin intermediate filaments and functions in pulmonary vascular endothelial cell migration via ROCK. *J. Cell. Physiol.* http://dx.doi.org/10.1002/jcp.25185 (2015).
47. Acar, M. *et al.* Deep imaging of bone marrow shows non-dividing stem cells are mainly perisinusoidal. *Nature* **526,** 126–130 (2015).
48. Mantel, C. R. *et al.* Enhancing hematopoietic stem cell transplantation efficacy by mitigating oxygen shock. *Cell* **161,** 1553–1565 (2015).
49. Shen, H. *et al.* An acute negative bystander effect of γ-irradiated recipients on transplanted hematopoietic stem cells. *Blood* **119,** 3629–3637 (2012).
50. Hu, L. *et al.* Antioxidant *N*-acetyl-l-cysteine increases engraftment of human hematopoietic stem cells in immune-deficient mice. *Blood* **124,** e45–e48 (2014).

Supplementary Information is available in the online version of the paper.

Acknowledgements We thank G. Karsenty and M. A. Lichtman for fruitful discussions and for critically reviewing the manuscript. We thank S. Méndez-Ferrer and M. Argueta Hernandez for assistance in studies involving MSPCs and nervous system elements. We thank Z. Porat for technical assistance with ImageStream analysis and R. Rotkopf for assistance with statistical data analysis. This study was partially supported by the Ministry of Science, Technology & Space, Israel and the DKFZ, Germany, grants from the Israel Science Foundation (851/13), the Ernest and Bonnie Beutler Research Program of Excellence in Genomic Medicine and EU FP7-HEALTH-2010 (CELL-PID #261387) (T.L.). Confocal studies were supported by the European Research Council Advanced Grant 339409, 'AngioBone' (R.H.A.). Intravital multiphoton studies were supported by NIH grants EB017274 and HL100402 (C.P.L. & D.T.S.).

Author Contributions T.I. designed and performed experiments, analysed data and wrote the manuscript; S.G-.C. helped in the design and execution of experiments and analysed data; J.A.S., A.S., and Y.J. designed and performed intravital related experiments, analysed data and helped with writing the manuscript; S.K.R. and A.P.K. designed and performed confocal related experiments and analysed data; G.L., I.M., M.G.P., A.K., A.L., and O.K. helped with experiments; K.G. participated in CFU-F and CFU-Ob related experiments; E.K. participated in metabolic ROS experiments, including plasma penetration and NAC treatment; A.K. participated in mice genotyping; G.S. helped and guided some intravital related experiments; J.M.B. and S.R. helped in design of endothelial-related studies; R.H.A helped and guided in design of confocal and *in vivo* endothelial related experiments; D.T.S. helped and guided design of *in vivo* intravital live imaging experiments and wrote the manuscript; and T.L. and C.P.L. guided and designed the research and wrote the manuscript.

Author Information Reprints and permissions information is available at www.nature.com/reprints. The authors declare no competing financial interests. Readers are welcome to comment on the online version of the paper. Correspondence and requests for materials should be addressed to T.L. (tsvee.lapidot@weizmann.ac.il) or C.P.L. (charles_lin@hms.harvard.edu).

METHODS

Data reporting. No statistical methods were used to predetermine sample size. The investigators were not blinded to allocation during experiments and outcome assessment

Animals. C57BL/6 (CD45.2) mice were purchased from Harlan Laboratories (Rehovot, Israel). B6.SJL (CD45.1) mice were bred in-house. Transgenic Ly6a(Sca-1)-EGFP mice and transgenic ROSA26-eYFP (Endo^{YFP}) reporter mice were purchased from Jackson Laboratories. Transgenic nestin-GFP mice were kindly provided by G. N. Enikolopov (Cold Spring Harbour Laboratory, USA). Transgenic c-Kit-EGFP mice were kindly provided by S. Ottolenghi (University of Milano-Bicocca, Italy). Transgenic VE-cadherin (Cdh5, PAC)-CreERT2 mice were kindly provided by R. H. Adams (Max Planck Institute for Molecular Biomedicine, Germany). Conditional mutants carrying *loxP*-flanked *Cxcr4* were provided by D. Scadden (Harvard University, Cambridge, USA). Conditional mutants carrying *loxP*-flanked *Fgfr1* and *Fgfr2* (*Fgfr1*/*Fgfr2*$^{lox/lox}$) mice were provided by S. Werner (Institute of Cell Biology, Switzerland) and by D. Ornitz (Washington University School of Medicine, USA). To induce endothelial-specific Cre activity and gene inactivation/expression, adult VE-cadherin(Cdh5, PAC)-CreERT2 mice interbred with *Cxcr4*$^{lox/lox}$ (Endo$^{\Delta Cxcr4}$) or *Fgfr1/2*$^{lox/lox}$ (Endo$^{\Delta Fgfr1/2}$) or with ROSA26-eYFP mice (Endo^{YFP}) were injected intraperitoneally (i.p.) with Tamoxifen (Sigma, T5648) at 1 mg per mouse per day for 5 days. Mice were allowed to recover for 4 weeks after tamoxifen injections, before euthanasia and experimental analysis. Mice carrying only VE-cadherin (Cdh5, PAC)-CreERT2 transgene or the *Cxcr4*$^{lox/lox}$/*Fgfr1/2*$^{lox/lox}$ mutations were used as wild-typecontrols to exclude non-specific effects of Cre activation or of floxed alleles mutation. The endothelial *Fgfr1/2* deletion was confirmed by qRT–PCR measurements of *Cxcr4* and *Fgfr1/2* mRNA from isolated BMECs.

Male and female mice at 8–12 weeks of age were used for all experiments. All mouse offspring from all strains were routinely genotyped using standard PCR protocols. Sample size was limited by ethical considerations and background experience in stem cell transplantation (bone marrow transplantation) which exists in the laboratory for many years and other published manuscripts in the stem cell field, confirming a significant difference between means. No randomization or blinding was used to allocate experimental groups and no animals were excluded from analysis. All mutated or transgenic mouse strains had a C57BL/6 background. All experiments were done with approval from the Weizmann Institute Animal Care and Use Committee. Mice that were maintained at the Weizmann Institute of Science were bred under defined flora conditions. Two-photon *in vivo* microscopy procedures that were performed in Harvard Medical School were approved by the Institutional Animal Care and Use Committee at Massachusetts General Hospital.

***In vivo* treatments.** AMD3100 (Sigma-Aldrich) 5 mg per kg was used to treat mice by subcutaneous (s.c.) injection. Mice were euthanized 30 min later.

Recombinant murine FGF-2 (ProSpec) 200 μg per kg was used to treat mice by i.p. injections for seven consecutive days.

Neutralizing rat anti-VE-cadherin antibodies or rat IgG (eBioscience) at 50 μg per mouse per day were used to treat mice by intravenous (i.v.) injections for 2 or 5 days.

Neutralizing mouse anti-CXCR4 antibodies (12G5 clone) or mouse IgG (eBioscience) at 50 μg per mouse were administered twice, with a 30 min interval, by intravenous (i.v.) injections.

To inhibit ROS production, the antioxidant *N*-acetyl-L-cysteine (NAC; Sigma-Aldrich) was administered by i.p. injection of 130 mg per kg for 2, 5 or 7 days. Mice were euthanized 2–4 h following the final injection.

Immunofluorescence. For standard and confocal fluorescent microscopy, femurs were fixed for 2 h in 4% paraformaldehyde, which was replaced and then the samples were washed with 30% sucrose, embedded in optimum cutting temperature compound, and then snap-frozen in *N*-methylbutane chilled in liquid nitrogen. Sections (5–10 μm) were generated with a CM1850 Cryostat (Leica) at −25 °C with a tungsten carbide blade (Leica) and a CryoJane tape transfer system (Instrumedics), and were mounted on adhesive-coated slides (Leica), fixed in acetone and air-dried. Sections were stained by incubation overnight at 4 °C with primary antibodies, followed by 1 h incubation of secondary antibody at room temperature and in some cases also nuclei labelling by Hoechst 33342 (Molecular Probes) for 5 min at room temperature. Standard analysis (5–6 μm sections) was performed with Olympus BX51 microscope and Olympus DP71 camera. Confocal analysis (10 μm sections) was performed using a Zeiss LSM-710 microscope. In some cases, for BMBV morphological and phenotypical confocal analysis, femurs and tibias were fixed for 2 h in 4% paraformaldehyde, decalcified with 0.5 M EDTA at 4 °C with constant shaking, immersed into 20% sucrose and 2% polyvinylpyrrolidone (PVP) solution for 24 hours, then embedded and frozen in 8% gelatin (porcine) in presence of 20% sucrose and 2% PVP. Sections (80–300 μm) were generated using low-profile blades on a CM3050 cryostat (Leica). Bone sections were air-dried, permeabilized for 10 min in 0.3% Triton X-100, blocked in 5% donkey serum at room temperature for 30 min, and incubated overnight at 4 °C with primary antibodies. Confocal analysis was performed using a Zeiss LSM-780 microscope. *Z*-stacks of images were processed and 3D-reconstructed with Imaris software (version 7.00, Bitplane). As previously described[4], tile scan images were produced by combining the signal of multiple planes along the Z-stalk of bone sections to allow visualization of the distinct types of bone marrow blood vessels and the cells in their surroundings. For the quantifications of blood vessel diameters, a region of 600–700 μm from the growth plate towards the caudal region was selected and diameters for arterial and sinusoidal blood vessels were calculated using ImageJ software on the high-resolution confocal images.

Primary and secondary antibodies and relevant information about them are indicated in Supplementary Table 1.

For *in vivo* ROS detection in bone marrow sections, mice were injected i.p. with hydroethidine (Life Technologies) 10 mg per kg, 30 min before euthanasia. For *in vivo* LDL-uptake detection in bone marrow sections, mice were i.v. injected with Dil-Ac-LDL (BTI) 20 μg per mouse, 4 h before euthanasia. Femurs were immediately collected and processed as mentioned earlier. Bone marrow section analysis for scoring ROS^{high} cells was performed using ImageJ software (Extended Data Fig. 1). Multiple sections (>16 per mouse) were generated and analysed from at least 4 mice per group of experimental procedure, in order to confirm biological repeats of the observed data. In some cases, images were processed to enhance the contrast in order to allow better evaluation of co-localization of cellular borders and markers.

Imaris, Volocity (Perkin Elmer), Photoshop and Illustrator (Adobe) software were used for image processing.

Intravital confocal and multiphoton microscopy. For blood vessel imaging in the calvarium of Sca-1-EGFP and nestin-GFP mice, we used a microscope (Ultima Multiphoton; Prairie Technologies) incorporating a pulsed laser (Mai Tai Ti-sapphire; Newport Corp.). A water-immersed 20× (NA 0.95) or 40× (NA 0.8) objective (Olympus) was used. The excitation wavelength was set at 850–910 nm. For intravital imaging, mice were anaesthetized with 100 mg ketamine, 15 mg xylazine and 2.5 mg acepromazine per kg. During imaging, mice were supplied with oxygen and their core temperature was maintained at 37 °C with a warmed plate. The hair on the skullcap was trimmed and further removed using urea-containing lotion and the scalp was incised at the midline. The skull was then exposed and a small steel plate with a cut-through hole was centred on the frontoparietal suture, glued to the skull using cyanoacrylate-based glue and bolted to the warmed plate. To visualize blood vessels, mice were injected i.v. with 2 μl of a 2 μM non-targeted nanoparticles solution (Qtracker 655, Molecular Probes). In some cases, mice were i.v. injected with Dil-Ac-LDL (BTI) 40 μg per mouse, 2 h before their imaging. We typically scanned a 50 μm-thick volume of tissue at 4 μm *Z*-steps. Movies and figures based on two-photon microscopy were produced using Volocity software (Perkin Elmer). For live imaging of blood vessels permeability and leukocyte bone marrow trafficking, a previously described experimental procedures and a home built laser-scanning multiphoton imaging system[29], were used with some modifications. Anaesthesia was slowly induced in mice via inhalation of a mixture of 1.5–2% isoflurane and O_2. Once induced, the mixture was reduced to 1.35% isoflurane. By making a U-shaped incision on the scalp, calvarial bone was exposed for imaging and 2% methocellulose gel placed on it for refractive index matching.

For bone marrow blood vessel permeability studies, mice were positioned in heated skull stabilization mount which allowed access to the eye for on-stage retro-orbital injection of 40–60 μl of 10 mg ml^{-1} 70 kDa rhodamine-dextran (Life Technologies). Nestin-GFP (excited at 840 nm) and confocal reflectance (at 840 nm) signals were used to determine a region of interest within the mouse calvarial bone marrow for measurement of permeability. Rhodamine-dextran was injected and was continuously recorded (30 frames per second) for the first 10 min after injection. After video acquisition, mice were removed from the microscope and euthanasized with CO_2. In some cases, following dextran clearance, the same mice were used for homing experiments to monitor leukocyte cell trafficking in regions and blood vessels that were defined as less or more permeable. For cell homing studies, mice were injected with 2×10^6 DiD-labelled (Life Technologies) lineage depleted immature haematopoietic progenitor cells (Miltenyi depletion) and with 2×10^6 DiI-labelled (Life Technologies) bone marrow MNC isolated from age matched C57BL/6 mice along with 150 μl of 2 nmol per 100 μl Angiosense 750EX (Perkin Elmer) fluorescent blood pool imaging agent, immediately before mounting the mice on a heated stage of a separate confocal/multiphoton microscope. Intravital images of the mouse bone marrow were collected for up to the first 3 h after injection of the cells. After imaging, the mice were removed from the microscope and euthanized with CO_2. Permeability, blood flow/shear rates and homing experiments were repeated, $n = 3$ mice each, measuring multiple blood vessels and events, each mouse regarded as an independent experiment, in order

to confirm biological repeats of the observed data. The contrast and brightness settings of the images in the figures were adjusted for display purposes only.

Permeability and cell homing quantification. For permeability studies, the RGB movies were separated into red (Rhodamine-Dextran), green (nestin-GFP), and blue (reflectance) grayscale image stacks. An image registration algorithm (Normalized Correlation Coefficient, Template Matching) was performed on the red stack using ImageJ (v. 1.47p) to minimize movement artefacts within the image stack. Manual selection of regions of interest (ROI) was performed immediately next to individual vessels within the focus. Permeability of the vessels was calculated using the following equation:

$$P = \frac{V}{A} \times \frac{dI}{dt} \times \frac{1}{I_{in} - I_{out}}$$

P is the permeability of the vessel, V is the volume of the ROI next to the vessel, A is the fractional surface area of the vessel corresponding to the ROI, dI/dt is the intensity of the dye in the ROI as a function of time, I_{in} is the intensity of the dye inside the corresponding vessel at the beginning of measurement, and I_{out} is the intensity of the dye in the ROI at the beginning of measurement. To calculate dI/dt for a given vessel, the change in intensity was measured within the ROI over time and linearly fit the first ~5–40 s of the data. The slope of this linear fit is dI/dt. The ROI intensity curve is only linear for the first 30–40 s, after which it begins to plateau. For cell homing, the number of stationary cells from the calvarial bone marrow images was counted and categorized into two groups: adherent and extravasated. We categorized both cells within the lumen of the vessel and cells in the process of transmigration in the adherent category. Maximum intensity projections of multiple z-stacks of images were used to count the number of cells in the two categories. When there was a gap between cells and vessels in the two-dimensional projection image, those cells were categorized as extravasated. If any part of a cell overlapped a vessel in the projection image, the corresponding three dimensional z-stack was viewed to determine if the cell had undergone extravasation. When it was unclear if a cell had extravasated, it was always categorized as adherent.

Blood flow speed and shear rate quantification. For the flow speed measurement, red blood cells (RBCs) were labelled with 15 μM CFSE for 12 min at 37 °C in PBS supplemented with 1 g per litre of glucose and 0.1% BSA. About 0.6 billion RBCs were injected (i.v). 40 μl of rhodamineB-dextran 70 kDa (10 mg ml^{-1}) was retro-orbitally injected immediately before imaging for visualizing bone marrow vasculature. Videos of confocal images of blood vessel (RhodamineB, excitation: 561 nm, emission: 573–613 nm) and labelled RBCs (CFDA-SE, excitation: 491 nm, emission: 509–547 nm) were taken with the speed of 120 frames per second. Individual RBCs were traced over a couple of frames. Total displacement of the RBCs was measured by ImageJ and the speed of blood flow was calculated by:

$$\frac{\text{Total displacement of RBC } (\mu\text{m})}{\text{Time } (=\text{number of frames } \times \frac{1}{120} \text{ sec})}$$

To calculate the shear rate, we assumed that the vessels were straight (straight cylinder) and the blood is an ideal Newtonian fluid with constant viscosity. Under these conditions, the shear rate (du/dr) can be calculated by $du/dr = 8 \times u/d$ (u is the average blood flow speed which was measured by tracing labelled RBCs and d is the diameter of the blood vessel as measured using ImageJ).

Flow cytometry. Immunostaining signal intensity was analysed with MacsQuant (Miltenyi, Germany) or with a FACS LSRII (BD Biosciences) with FACSDiva software, data were analysed with FlowJo (Tree Star). Data of the expression of molecules by cells was analysed and presented as MFI (mean fluorescent intensity). To acquire single bone marrow cell suspensions, freshly isolated bones were cleaned, flushed and crushed using liver digestion medium (LDM, Invitrogen) supplemented with 0.1% DNaseI (Roche) and further digested for 30 min at 37 °C, under shaking conditions. Following the incubation time, cells were filtered and washed extensively. To isolate and acquire mononuclear cells (MNC) from the peripheral blood PB, blood was collected from the heart using heparinized syringes and MNC were separated using Lymphoprep (Axis-Shield) according to the manufacturer's instructions. Isolated bone marrow and peripheral blood MNC cells underwent red blood cell lysis (Sigma) before staining. Cells were stained for 30 min at 4 °C in standard flow cytometry buffer with primary antibodies and, where indicated, with secondary antibodies. Information about the primary and secondary antibodies can be found in the antibody information (Supplementary Table 1).

For antigens that required intracellular staining, cell surface staining was followed by cell fixation and permeabilization with the Cytofix/Cytoperm kit following the manufacturer's instructions (BD Biosciences). In case of internal GFP labelled cells, cells were fixed for 20 min with 4% PFA at room temperature, washed and incubated at room temperature for 1 h in 30% sucrose. Cells were washed with flow cytometry buffer and further permeabilized. For intracellular ROS detection, cells were incubated for 10 min at 37 °C with 2 μM hydroethidine (Life Technologies). For glucose uptake detection, cells were incubated for 30 min at 37 °C with the glucose analogue 2-NBDG (Life Technologies). For detection of apoptotic cells, cells were resuspended in annexinV binding buffer (BioLegend) and stained with Pacific Blue AnnexinV (BioLegend).

ImageStream analysis. Bone marrow cells were enriched for the lineage negative population, prepared as indicated for flow cytometry and analysed using an ImageStreamX (Amnis) machine. Samples were visualized and analysed for the expression of markers and antigens with IDEAS 4.0 software (Amnis). Single-stained control cells were used to compensate fluorescence between channel images. Cells were gated for single cells with the area and aspect ratio features or, for focused cells, with the Gradient RMS feature. Cells were then gated for the selection of positively stained cells only with their pixel intensity, as set by the cutoff with IgG and secondary antibody control staining. At least 5 samples from 5 mice were analysed to confirm biological repeats of observed data.

Calcitonin and PTH ELISA kit assays. Detection of mouse calcitonin (Cusabio) and mouse PTH (Cloud-Clone Corp.) levels in bone marrow supernatants was performed according to the manufacturer's instructions.

CFU assays. CFU-GM and CFU-F assays were previously described[34]. For CFU-Ob assay (also known as mineralized nodule formation assay), CFU-F medium was supplemented with 50 μg ml^{-1} ascorbic acid and with 10 mM β-glycerophosphate. After 3 weeks, cultures were washed, fixed and stained using Alizarin red for mineralized matrix. The area of mineralized nodules per cultured well was quantified based on image analysis using ImageJ.

***In vitro* assays.** Bone marrow cells were isolated after sterile bone flushing, crushing and digestion (as previously described). After washing, total bone marrow cells were incubated in medium supplemented with or without 25% blood plasma or supplemented with 20 ng ml^{-1} TGF-β1 (ProSpec) for 2 h. Plasma was isolated and collected from the upper fraction acquired from the peripheral blood after 5 min centrifugation at 1,500 r.p.m.

***In vivo* Evans blue dye bone marrow penetration assay.** Bone marrow vascular endothelial barrier function was assessed using the Evans Blue Dye (EBD) assay. Evans Blue (Sigma-Aldrich) 20 mg per kg was injected i.v. 4 h before mice were euthanized. In each experiment, a non-injected mouse was used for control blank measurements. Subsequently, mice were perfused with PBS via the left ventricle to remove intravascular dye. Femurs were removed and formamide was used for bone flushing, crushing and chopping. EBD was extracted in formamide by incubation and shaking of flushed and crushed fractions, overnight at 60 °C. After 30 min centrifugation at 2,000g, EBD in bone marrow supernatants was quantitated by dual-wavelength spectrophotometric analysis at 620 nm and 740 nm. This method corrects the specimen's absorbance at 620 nm for the absorbance of contaminating haem pigments, using the following formula: corrected absorbance at 620 nm = actual absorbance at 620 nm – (1.426(absorbance at 740) + 0.03). Samples were normalized by subtracting control measurements. Levels of EBD bone marrow penetration per femur were expressed as OD_{620}/femur and the fold change in EBD bone marrow penetration was calculated by dividing the controls OD_{620}/femur from the treated OD_{620}/femur in each experiment. Finally, values were normalized per total protein extract as determined by Bradford assay per sample.

Transplantation assays. For competitive LTR assay, B6.SJL (CD45.1) recipient mice were lethally irradiated (1,000 cGy from a caesium source) and injected 5 h later with 2×10^5 donor-derived (C57BL/6 background, CD45.2) bone marrow cells or with 500 μl of donor-derived whole blood together with 4×10^5 recipient derived (CD45.1) bone marrow cells. Recipient mice were euthanized 24 weeks after transplantation to determine chimaerism levels using flow cytometry analysis. For calculation of competitive repopulating units (CRU), recipient mice were transplanted with limiting dilutions of donor derived bone marrow cells (2.5×10^4 to 2×10^5) together with 2×10^5 recipient derived bone marrow cells. Mice were euthanized after 24 weeks and multi-lineage myelo-lymphoid donor derived contribution in the peripheral blood was assessed using flow cytometry analysis. HSC-CRU frequency and statistical significance was determined using ELDA software (http://bioinf.wehi.edu.au/software/elda/).

***In vivo* homing assay.** Lineage negative cells were enriched from total bone marrow cells, taken from c-Kit-EGFP mice, using mouse lineage depletion kit (BD) according to the manufacturer's instructions. Non-irradiated recipient mice were transplanted by i.v. injection with 2×10^6 c-Kit-EGFP-labelled Lin$^-$ cells. Recipient mice were euthanized 4 h after transplantation. Bone marrow cells were isolated from femurs and stained for flow cytometry as described above. Femur cellularity was determined in order to calculate the number of homed CD34$^-$/LSK HSPC per femur.

Quantitative real-time RT–PCR to BMECs. For magnetic isolation of BMECs, freshly recovered bones were processed under sterile conditions as described for BMECs flow cytometry analysis, and post-digestion incubated with biotin rat

anti-mouse CD31 antibodies (BD pharmigen) for 30 min at 4 °C. Next, cells were washed and incubated with streptavidin particles plus (BD IMag) for 30 min at 4 °C. Positive selection was performed using BD IMagnet (BD) according to the manufacturer's instructions (BD Biosciences). BD IMag buffer (BD) was used for washing and for antibodies dilution. Isolated cells were seeded on fibronectin (Sigma-Aldrich) coated wells and cultured overnight in EBM-2 medium (Lonza) supplemented with EGM-2 SingleQuots (Lonza) at 37 °C 5% CO_2. Non-adhesive cells were removed and adherent cells were collected using accutase (eBioscience). Flow cytometry was applied to confirm endothelial identity and >90% purity of recovered cells. BMEC were further processed to isolate RNA. Total RNA was isolated using TRI-Reagent (Sigma-Aldrich) according to the manufacturer's protocol. An aliquot of 2 μg of total RNA was reverse-transcribed using Moloney murine leukaemia virus reverse transcriptase (Promega, Madison, WI) and oligo-dT primers (Promega). Quantitative reverse transcribed–polymerase chain reaction (qRT–PCR) was done using the ABI 7000 machine (Applied Biosystems, Foster City, CA) with SYBR Green PCR Master Mix (Applied Biosystems). Comparative quantization of transcripts was assessed relative to hypoxanthine phosphoribosyl transferase (*Hprt*) levels and amplified with appropriate primers. Primer sequences used were as follows (mouse genes): *Cxcr4* forward 5′- ACGGCTGTAGAGCGAGTGTT-3′; reverse 5′- AGGGTTCC TTGTTGGAGTCA-3′; *Fgfr1* forward 5′-CAACCGTGTGACCAAAGTGG-3′; reverse 5′-TCCGACAGGTCCTTCTCCG-3′; *Fgfr2* forward 5′-ATCCCC CTGCGGAGACA-3′; reverse 5′-GAGGACAGACGCGTTGTTATCC-3′; *Hprt* forward 5′-GCAGTACAGCCCCAAAATGG-3′; reverse 5′-GGTC CTTTTCACCAGCAAGCT-3′.

Statistical analysis. All statistical analyses were conducted with Prism 4.0c version or Excel ($*P < 0.05$, $**P < 0.01$, $***P < 0.005$; NS, not significant). All data are expressed as mean ± standard error (s.e.m) and all *n* numbers represent biological repeats. Unless indicated otherwise in figure legends, a Student's two-tailed unpaired *t*-test was used to determine the significance of the difference between means of two groups. One-way ANOVA or two-way ANOVA was used to compare means among three or more independent groups. Bonferroni post-hoc tests were used to compare all pairs of treatment groups when the overall *P* value was <0.05. A normal distribution of the data was tested using the Kolmogorov–Smirnov test if the sample size allowed. If normal-distribution or equal-variance assumptions were not valid, statistical significance was evaluated using the Mann–Whitney test and the Wilcoxon signed rank test. Animals were randomly assigned to treatment groups. Tested samples were assayed in a blinded fashion.

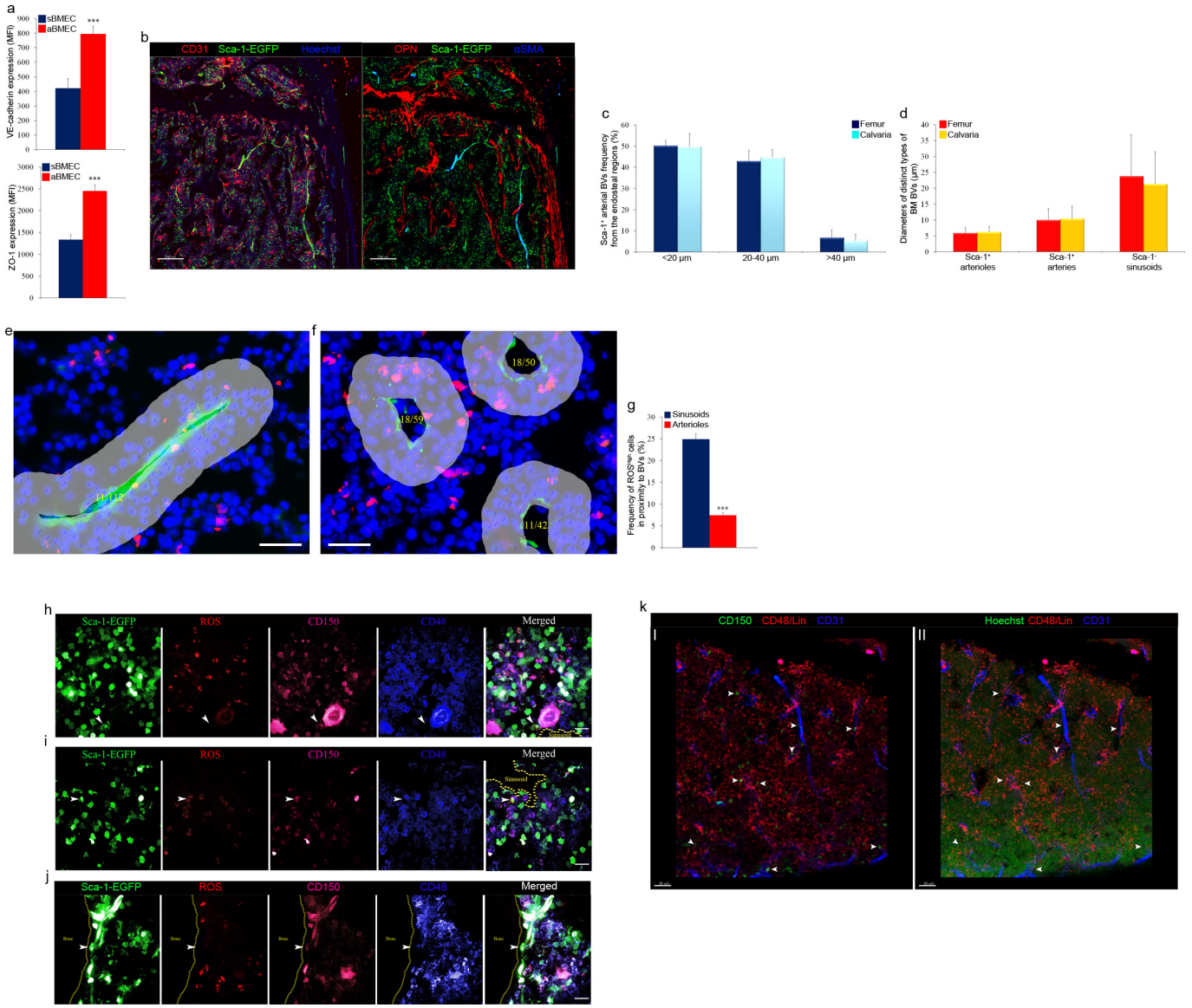

Extended Data Figure 1 | Properties of distinct types of bone marrow blood vessels and cells in their microenvironment. a, Flow cytometry quantitative analysis of VE-cadherin and ZO-1 MFIs by BMEC sub-populations. Mean ± s.e.m., $n = 9$ mice from three independent experiments. Two-tailed Student's *t*-test; $^{***}P < 0.005$. **b**, Representative confocal image showing CD31 (red) and Sca-1$^+$ (green) arterial blood vessels on proximity to endosteal regions in the metaphysis and representative confocal image of endosteal regions in the metaphysis showing Sca-1$^+$ (green) arterial blood vessels, αSMA$^+$ (blue) pericytes, and OPN (red) for endosteal borders. Scale bars indicate 200 μm. **c**, Frequencies of Sca-1$^+$ arterial blood vessels distribution among zones representing growing distances from the endosteum in the calvaria and femur. **d**, Average diameters of distinct types of blood vessels in the clavarial and femoral marrow. **e**, **f**, Representative images of arterial blood vessel (green, left) and of sinusoidal blood vessels (green, right) indicating how the frequency of ROS^{high} cells around these blood vessels was scored. The grey-masked areas surrounding the blood vessels indicate the region of distance <20 μm from the blood vessels. Odd numbers (1, 3, and 5) tag the nuclei of cells (blue) found in the region of interest, while even numbers (2, 4, and 6) tag ROS^{high} (red) cells in the region of interest. ImageJ cell counter plugin was used to analyse and score the number of total cells and ROS^{high} cells in the region of interest. Yellow numbers in the centre of the blood vessels indicate how many ROS^{high} cells are scored out of total cells. Scale bar indicates 20 μm. **g**, Frequency of ROS^{high} cells scored among total bone marrow cells found in proximity (<20 μm) to different bone marrow blood vessels. Mean ± s.e.m., $n = 24$ bone marrow sections were analysed from $n = 6$ mice. Two-tailed Student's *t*-test; $^{***}P < 0.005$. **h**–**k**, White arrowheads indicate for SLAM HSPC **h**, Representative confocal images with ROS probe (red) of ROS$^{low/-}$, CD150$^+$ (pink)/CD48$^-$ (blue) SLAM HSPC, found away (>20 μm) from Sca-1$^+$ (green) endosteal blood vessels, neighbouring a megakaryocyte. Yellow dashed line indicates sinusoidal borders. Scale bar indicates 20 μm. **i**, Representative confocal images of ROS^{high} (red), CD150$^+$ (pink) and CD48$^-$ (blue) SLAM-HSPC, found away (>20 μm) from Sca-1$^+$ (green) endosteal blood vessels, surrounded by mature haematopoietic cells. Yellow dashed line indicates sinusoidal borders. Scale bar indicates 20 μm. **j**, Representative confocal images of cells with ROS^{high} (red) levels among CD150$^+$ (pink) and CD48$^-$ (blue) SLAM-HSPC neighbouring (<20 μm) Sca-1$^+$ (green) the endosteal arteriole. Scale bar indicates 20 μm. **k**, Representative tile scan confocal images of bone marrow merged Z-stalk showing (I) CD31$^+$ blood vessels (blue) and their neighbouring CD150$^+$ (green) CD48/Lin (red) negative SLAM HSPC. (II) Cells nuclei are visualized (green) together with CD48/Lin (red) and CD31$^+$ blood vessels (blue). Scale bars indicate 30 μm.

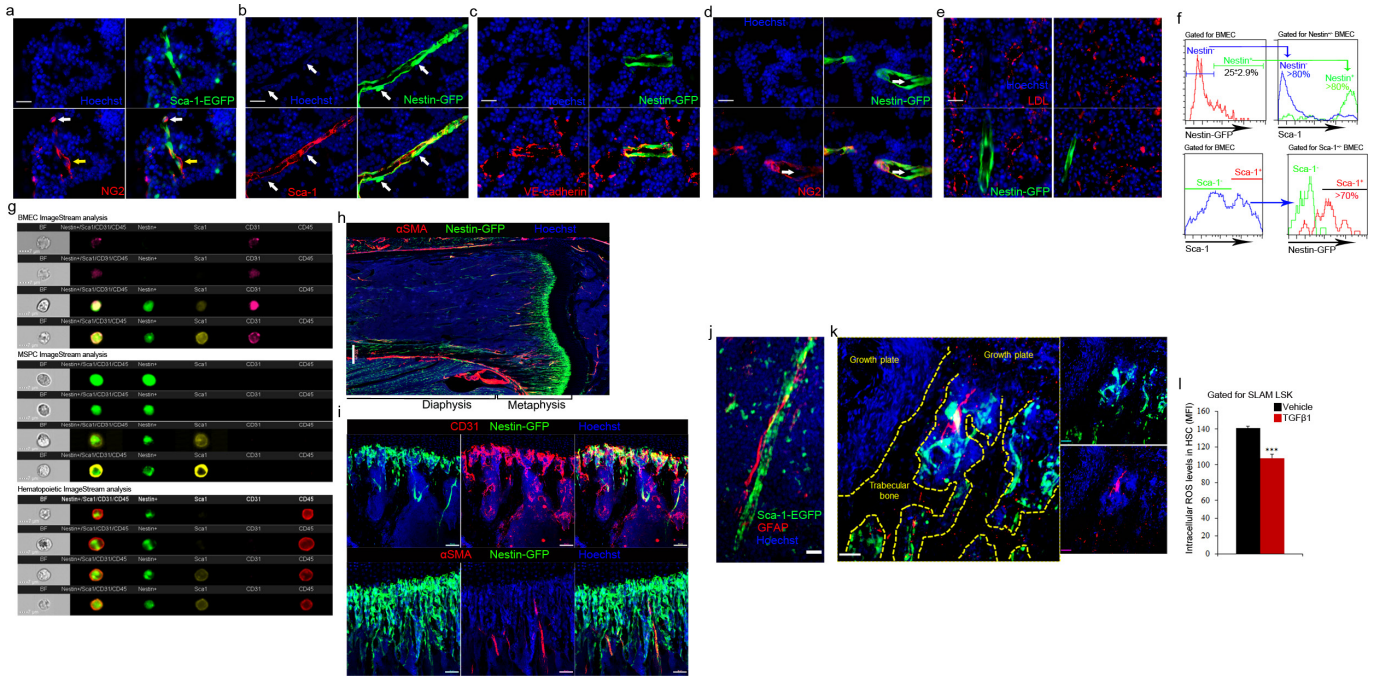

Extended Data Figure 2 | Different populations of nestin-expressing bone marrow cells are associated with nestin-expressing arterioles. **a**, Representative fluorescence images of Sca-1$^+$ (green) blood vessels and their neighbouring NG2$^+$ (red) MSPCs. NG2$^+$ MSPCs were either negative (yellow arrow) or positive (white arrow) for Sca-1 expression. Scale bar indicates 20 μm. **b**, Representative fluorescence images of Sca-1$^+$ (red) blood vessels and nestin-GFP labelling (green) blood vessels and MSPCs (white arrows). Scale bar indicates 20 μm. **c**, Representative fluorescence images of nestin$^+$ (green) blood vessels and VE-cadherin (red) staining, showing that nestin$^+$ blood vessel structures are co-stained with VE-cadherin while neighbouring sinusoids are VE-cadherin$^+$/nestin$^-$. Scale bar indicates 20 μm. **d**, Representative fluorescence images of nestin$^+$ (green) blood vessels and their neighbouring NG2$^+$ (red) MSPCs. NG2$^+$/nestin$^+$ MSPCs surrounded NG2$^-$/nestin$^+$ aBMECs with elongated nuclei (white arrow). Scale bar indicates 20 μm. **e**, Representative fluorescence images of large- and small-diameter nestin$^+$ (green) blood vessels and blood vessels positive for LDL (red) uptake, indicating that nestin$^+$ labels arteries and arterioles but not sinusoids. Scale bar indicates 20 μm. **f**, Representative flow cytometry histogram plots for gated BMECs, showing nestin-GFP expression on BMEC subpopulation which is Sca-1$^+$ or nestin-GFP expression by Sca-1$^{+/-}$ BMEC subpopulation. Mean ± s.e.m., $n = 6$ mice from three independent experiments. **g**, Representative ImageStream images of CD45$^-$CD31$^+$Sca-1$^-$nestin$^-$ sBMECs and CD45$^-$CD31$^+$Sca-1$^+$nestin$^+$ aBMECs, CD45$^-$CD31$^-$ Sca-1$^{+/-}$nestin$^+$ MSPCs, and CD45$^+$CD31$^-$Sca-1$^{+/-}$nestin$^+$ haematopoietic cells. **h**, Representative confocal tile scan of nestin-GFP (green) femur stained with αSMA (red). Scale bar indicates 200 μm. **i**, Representative confocal images of endosteal regions in the metaphysis showing αSMA (red) enwrapped nestin$^+$ (green) andCD31$^+$ (white) arterial blood vessels branching into smaller endosteal nestin$^+$CD31$^+$ arterioles which are not associated with αSMA$^+$ pericytes. Endosteal nestin$^+$ blood vessels are surrounded by nestin$^+$ MSPCs. Scale bars indicate 50 μm. **j**, **k**, Representative confocal images of diaphysial area (**j**) and metaphysial area (**k**) showing GFAP (red, Schwann cell marker) fibres associated with Sca-1$^+$ (green) arterial blood vessel (**j**) or with Sca-1$^+$ endosteal arterioles (**k**). Scale bar indicates 50 μm (**j**) and 100 μm (**k**). **l**, Bone marrow cells were incubated with 20 ng ml^{-1} TGFβ1 or vehicle for 2 h. ROS MFI levels in bone marrow SLAM HSPCs were determined by flow cytometry quantitative analysis. Mean ± s.e.m., $n = 9$ repeats in triplicates from three independent experiments. Two-tailed Student's *t*-test; $^{***}P < 0.005$.

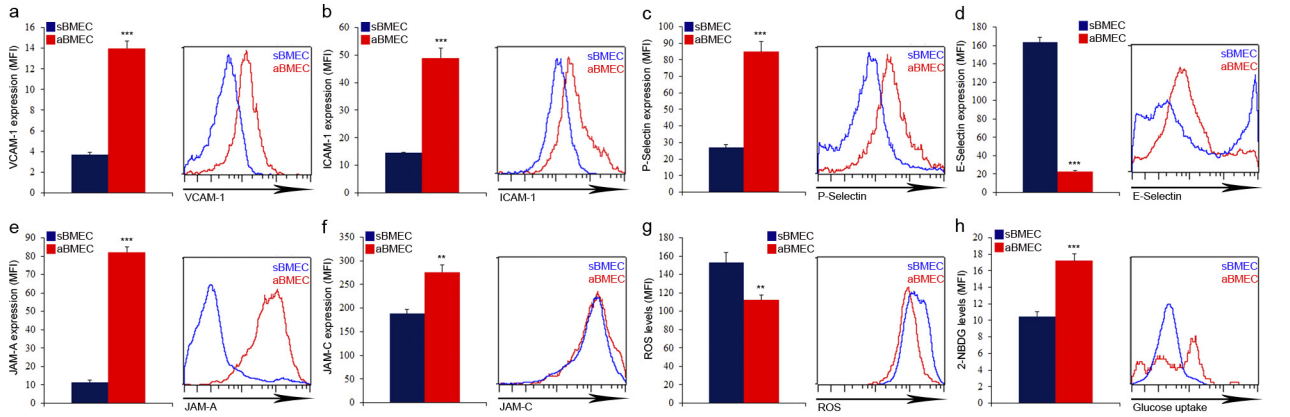

Extended Data Figure 3 | Expression pattern of molecules involved in cellular trafficking by distinct types of blood vessels. a–h, Expression levels (MFI) of indicated surface or intracellular molecules by distinct types of BMEC as measured by flow cytometry analysis. Mean ± s.e.m., $n = 8$ Sca-1-EGFP and wild-type mice from two independent experiments). Two-tailed Student's t-test; $^{**}P < 0.01$, $^{***}P < 0.005$.

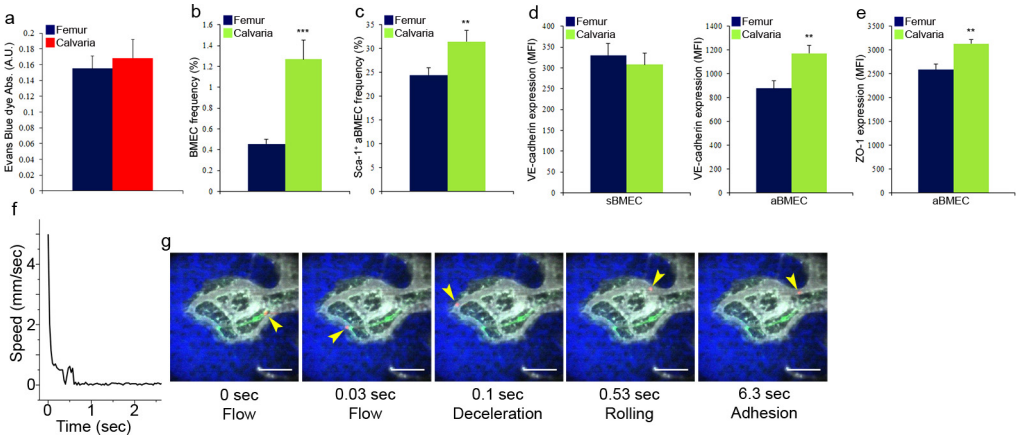

Extended Data Figure 4 | Femural and calvarial comparison and monitoring of calvarial trafficking. a, Evans blue dye (EBD) absorbance following extraction from the femurs or calvarias, was measured using spectrophotometric analysis at 620 nm and 740 nm and normalized to total protein content per femur (Bradford). Mean ± s.e.m., $n = 6$ mice from two independent experiments. **b**–**e**, Mean ± s.e.m., $n = 8$ mice from two independent experiments. Two-tailed Student's t-test; $^{**}P < 0.01$, $^{***}P < 0.005$. **b**, Total BMEC frequency as determined by flow cytometry analysis. **c**, Sca-1^{+} aBMEC frequency as determined by flow cytometry analysis. **d**, **e**, VE-cadherin and ZO-1 expression (MFI) on distinct types of BMECs as determined by flow cytometry analysis. **f**, A representative plot showing the flow speed of an HSPC passing through a network of nestin-GFP$^{+/-}$ blood vessels as a function of time. Note that the cell temporarily stops within a sinus at ~0.4 s and slowly roles until it adheres again at ~0.7 s. **g**, Snapshot images from 0, 0.03, 0.10, 0.53, and 6.3 s taken from Supplementary Video 5. Nestin-GFP (green), HSPC (red), blood vessels (grey), and bone (blue) are displayed. The cell is overlaid on the pre-acquired nestin-GFP, blood vessels, and bone images. Yellow arrows indicate for the location of the trafficking HSPC. Scale bars indicate 100 μm.

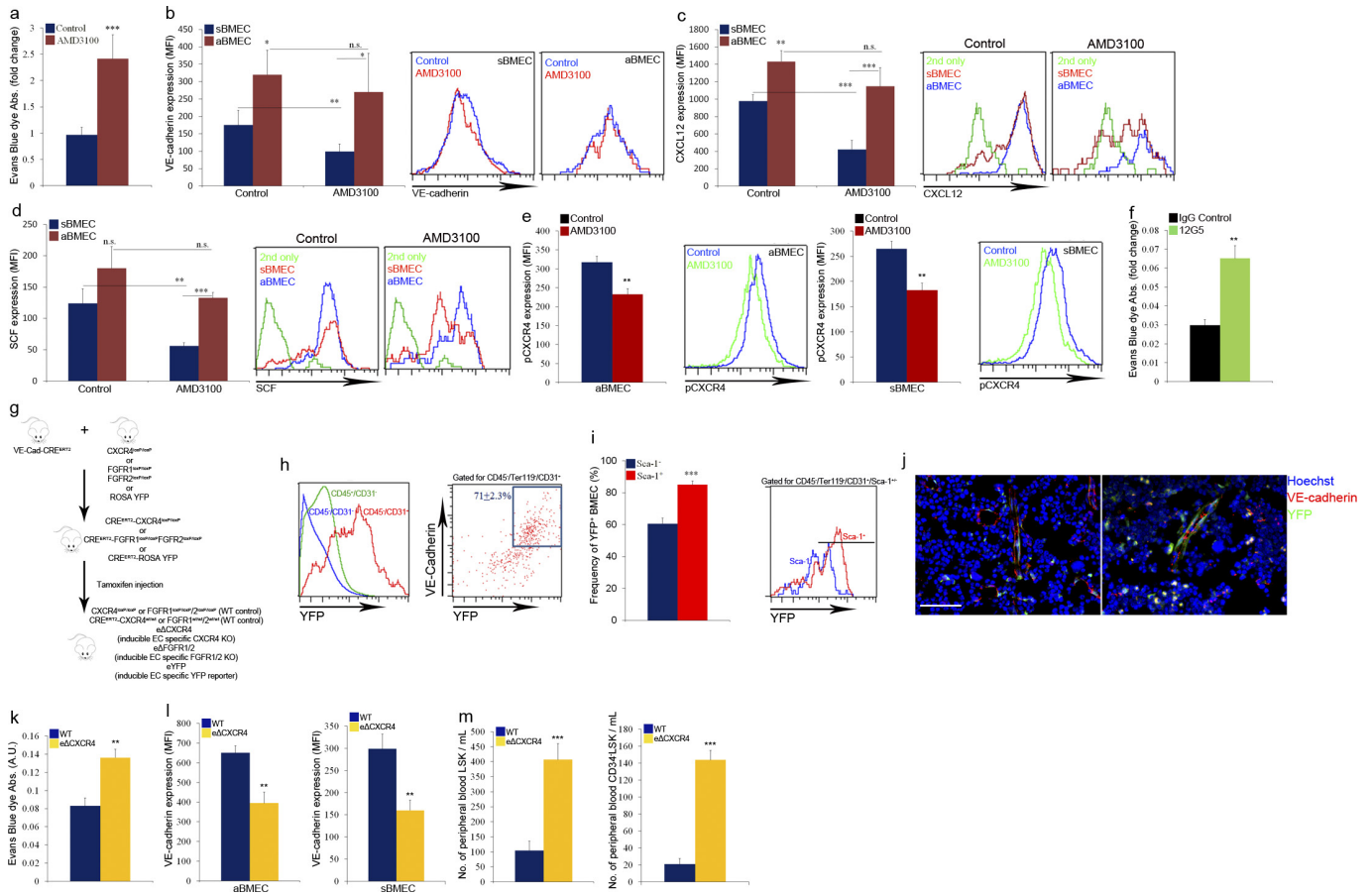

Extended Data Figure 5 | Properties of distinct types of bone marrow blood vessels under HSPC mobilization conditions and the role of the endothelial CXCL12–CXCR4 axis. a–**e**, C57BL/6 or nestin-GFP mice received a single injection of AMD3100 (5 mg per kg) and were analysed 5 min (for pCXCR4) or 30 min later. Mean ± s.e.m., $n = 7$ mice from three independent experiments. Two-way ANOVA with Bonferroni's multiple comparison post-hoc test; $^{*}P < 0.05$, $^{**}P < 0.01$, $^{***}P < 0.005$. **a**, Evans blue dye (EBD) absorbance following EBD (30 mg per kg) injection together with AMD3100. **b**–**d**, Flow cytometry quantitative analysis and representative histogram plots of VE-cadherin, membrane-bound CXCL12, and membranal SCF MFIs. **e**, Intracellular CXCR4 phosphorylation (pCXCR4) levels (MFI) in distinct types of BMECs as measured by flow cytometry analysis and representative histogram plots. **f**, C57BL/6 mice received two injections (30 min interval) of 50 μg 12G5 CXCR4 neutralizing antibodies or IgG control followed by EBD injection. EBD absorbance following extraction from the femur was measured using spectrophotometric analysis at 620 nm and 740 nm. Mean ± s.e.m., $n = 6$ mice from two independent experiments. Two-tailed Student's *t*-test, $^{**}P < 0.01$. **g**, Endothelial cell (EC)-specific inducible deletion of *Cxcr4* (Endo$^{\Delta Cxcr4}$) or *Fgfr1/2* (Endo$^{\Delta Fgfr1/2}$) in mice. Mice harbouring *loxP* sites flanking *Cxcr4* or *Fgfr1* and *Fgfr2* genes were crossed with a mouse line with endothelial-cell-specific VE-cadherin promoter-driven CreERT2 (VE-cadherin (Cdh5, PAC)-CreERT2). Specificity of VE-cadherin (Cdh5, PAC)-CreERT2 was validated in reporter mice carrying enhanced YFP protein following floxed stop codon (Endo^{YFP}). *Cxcr4* or *Fgfr1/2* deletion or YFP expression in endothelial cells was induced by tamoxifen injection. Mouse analysis was performed 4 weeks after tamoxifen-induced Cre activity. Mice carrying only the *Cxcr4*$^{lox/lox}$ or *Fgfr1/2*$^{lox/lox}$ mutations or VE-cadherin (Cdh5, PAC)-CreERT2 transgene served as controls. **h**–**j**, Mean ± s.e.m., $n = 12$ mice from four independent experiments. Two-tailed Student's *t*-test; $^{***}P < 0.005$. **h**, Representative flow cytometry histogram and dot plots confirming BMEC specific induction of Cre activity by exclusive expression of YFP in ~70% of BMEC. **i**, Frequency of YFP expression and representative histogram plot, among BMEC sub-populations, was determined by flow cytometry quantitative analysis 4 weeks after tamoxifen induction of Cre activity. Note higher Cre activity, indicated by higher YFP signal, in aBMECs. Black line indicates for a positive signal region. **j**, Fluorescent representative images of YFP expression by distinct BMBVs (sinusoids and arteries). **k**–**m**, Tamoxifen-treated wild-type and Endo$^{\Delta Cxcr4}$ mice were allowed to recover for 4 weeks before studies. Mean ± s.e.m., $n = 9$ mice from three independent experiments. Two-tailed Student's *t*-test; $^{*}P < 0.05$, $^{**}P < 0.01$, $^{***}P < 0.005$. **k**, EBD absorbance in wild-type and Endo$^{\Delta Cxcr4}$ mice. **l**, Flow cytometry quantitative analysis of VE-cadherin MFI on BMEC from wild-type and Endo$^{\Delta Cxcr4}$ mice. **m**, Flow cytometry quantitative analysis of blood LSK HSPCs and CD34^{-}LSK HSPCs of wild-type or Endo$^{\Delta Cxcr4}$ mice.

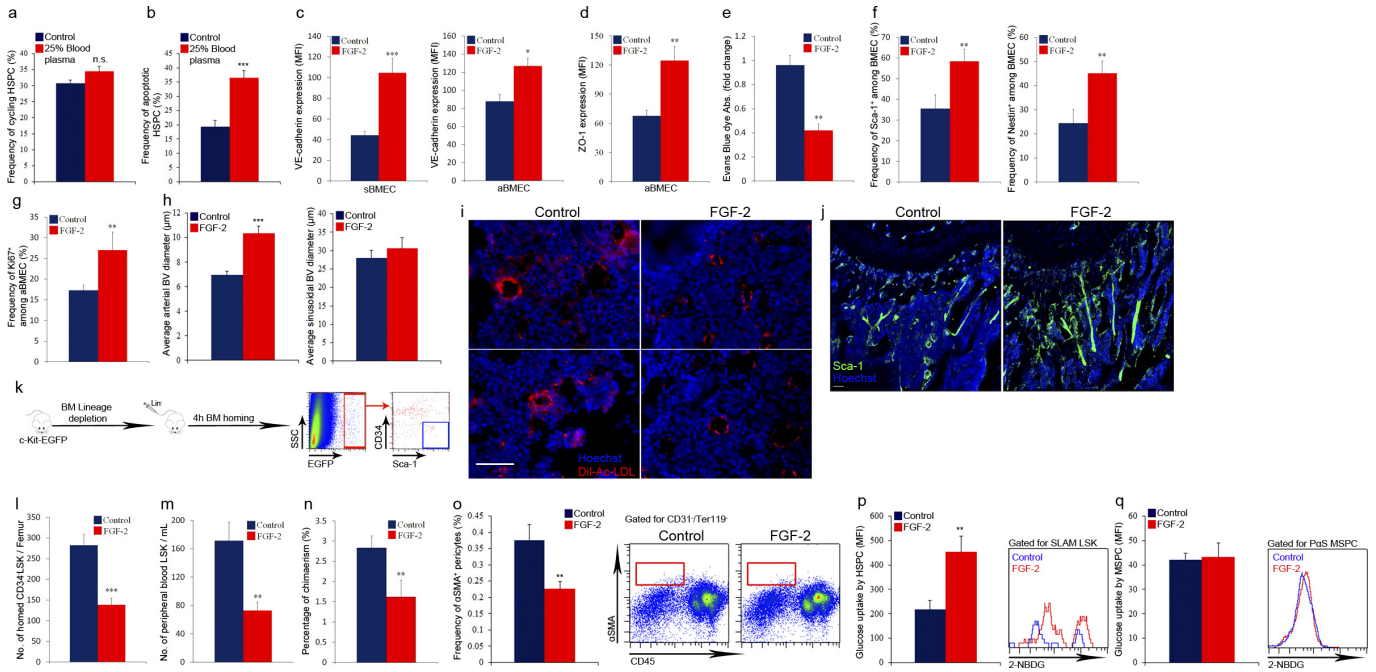

Extended Data Figure 6 | FGF-2 administration remodels the bone marrow vasculature and the stromal compartment while retaining HSPCs in the bone marrow. a, **b**, Bone marrow cells were incubated for 2 h with (25% blood plasma) or without (control) peripheral blood plasma. Mean ± s.e.m., $n = 9$ repeats from three independent experiments. Two-tailed Student's *t*-test; $***P < 0.005$. **a**, Frequencies of cycling Ki67$^+$ SLAM LSK HSPC. **b**, Frequencies of apoptotic annexinV$^+$ SLAM LSK HSPC. **a**–**f**, C57BL/6 or nestin-GFP mice were treated with FGF-2 (200 μg per kg) for 7 days. Mean ± s.e.m., $n = 9$ mice from three independent experiments. Two-tailed Student's *t*-test; $*P < 0.05$, $***P < 0.005$, $**P < 0.01$. **c**, **d**, Quantitative analysis of VE-cadherin and ZO-1 MFIs on BMECs. **e**, EBD absorbance. **f**, **g**, Flow cytometry quantitative analysis of BMEC frequencies expressing Sca-1, nestin and intracellular Ki67 cell cycling markers. **h**, Diameters of distinct types of bone marrow blood vessels in the metaphysis region as determined by ImageJ software analysis of high-resolution confocal images. **i**, Fluorescent representative images of LDL (red) uptake by sinusoidal BMEC and other bone marrow cells following diffusion into the parenchymal marrow. Note lower LDL uptake and diffusion following FGF-2 treatment. Scale bar indicates 20 μm. **j**, Representative confocal images of Sca-1$^+$ (green) arterial blood vessels in the metaphysis region. Note higher abundance of arterial blood vessels following FGF-2 treatment. Scale bar indicates 200 μm. **k**, For the homing assay, bone marrow cells from c-Kit-EGFP labelled mice were lineage depleted, and transplanted to the indicated recipient mice. Four hours after transplantation, bones from recipient mice were recovered, flushed and crushed, and the numbers of homed Lin$^-$c-Kit-EGFP$^+$Sca-1$^+$ CD34$^-$ HSPCs were determined per femur by flow cytometry quantitative analysis. **l**–**q**, Mice were treated with FGF-2 (200 μg per kg) for 7 days. Mean ± s.e.m., unless indicated otherwise $n = 12$ mice from three independent experiments. Two-tailed Student's *t*-test; $**P < 0.01$, $***P < 0.005$. **l**, HSPC homing per femur. Mean ± s.e.m., $n = 8$ mice from three independent experiments. **m**, Numbers of LSK HSPCs in the blood. **n**, Levels of chimaerism indicating LTR-HSC contribution from blood transplant. Mean ± s.e.m., $n = 20$ mice from two independent experiments. **o**, Frequencies and representative density plots of bone marrow αSMA$^+$ pericytes as determined by flow cytometry analysis. **p**, **q**, Expression levels (MFI) and representative histograms of glucose uptake by HSPCs and MSPCs, respectively, were determined by flow cytometry analysis.

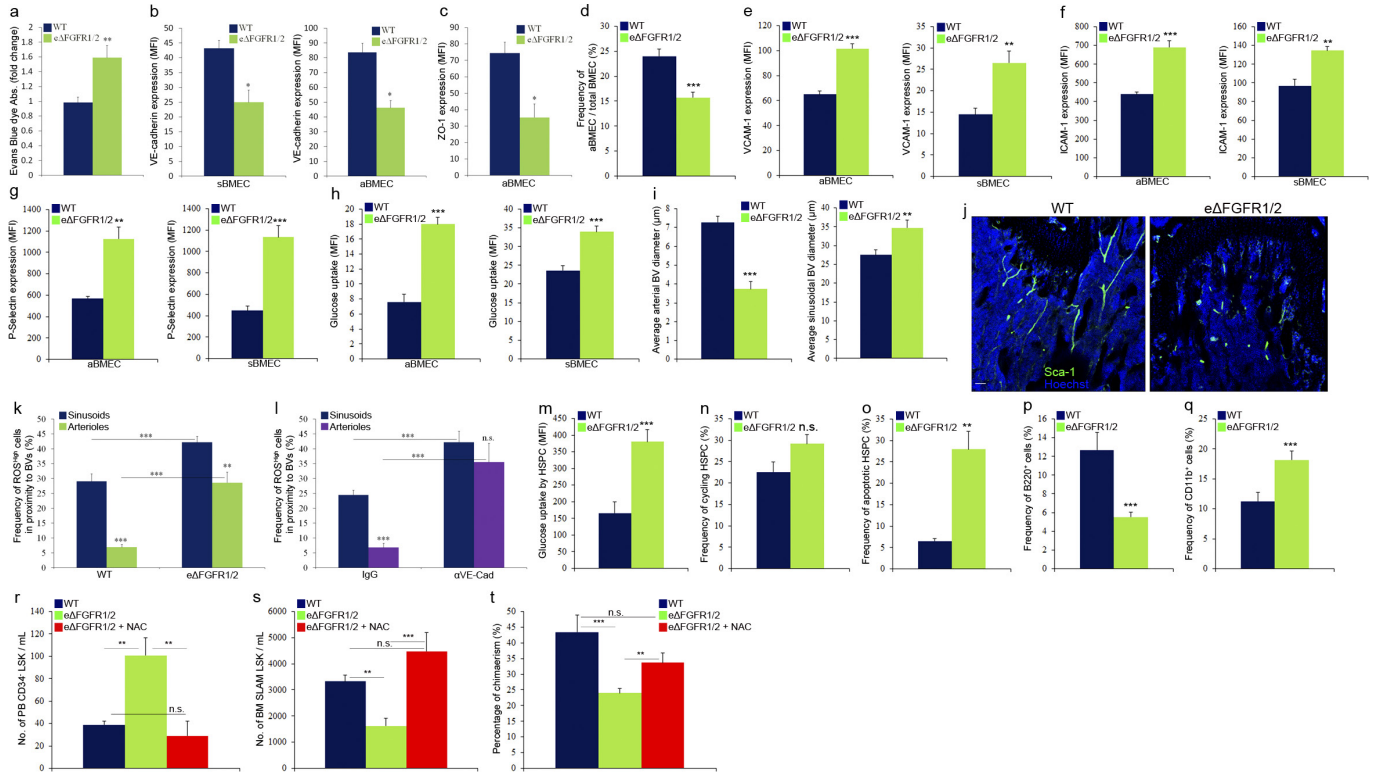

Extended Data Figure 7 | Genetic breaching of the endothelial barrier remodels the bone marrow vasculature and the stromal compartment while enhancing HSPC egress in a ROS dependent manner.
a, EBD absorbance. Mean ± s.e.m., $n = 6$ mice from three independent experiments. Two-tailed Student's *t*-test; $^{**}P < 0.01$. **b**, **c**, Quantitative analysis of VE-cadherin and ZO-1 MFIs on BMEC. Mean ± s.e.m., $n = 6$ mice from three independent experiments. Two-tailed Student's *t*-test; $^{*}P < 0.05$. **d**–**h**, Flow cytometry quantitative analysis of BMEC frequencies, surface and intracellular molecules expression (MFI), in wild-type or Endo$^{\Delta Fgfr1/2}$ mice. Mean ± s.e.m., $n = 9$ mice from three independent experiments. Two-tailed Student's *t*-test; $^{**}P < 0.01$, $^{***}P < 0.005$. **i**, Diameters of distinct types of bone marrow blood vessels in the metaphysis region as determined by ImageJ software analysis of high-resolution confocal images. **j**, Representative confocal representative images of Sca-1^{+} (green) arterial blood vessels in the metaphysis region. Note lower abundance of arterial blood vessels in Endo$^{\Delta Fgfr1/2}$ mice. Scale bar indicates 200 μm. **k**, **l**, Mean ± s.e.m., $n = 16$ bone marrow sections were analysed from $n = 4$ mice. Two-way ANOVA with Bonferroni's multiple comparison post-hoc test; $^{**}P < 0.01$, $^{***}P < 0.005$). **k**, Frequency of ROS^{high} cells scored among total bone marrow cells found in proximity (<20 μm) to different bone marrow blood vessels, in wild-type or Endo$^{\Delta Fgfr1/2}$ mice. **l**, Frequency of ROS^{high} cells scored among total bone marrow cells found in proximity (<20 μm) to different bone marrow blood vessels, in C57BL/6 mice treated with neutralizing rat anti-VE-cadherin antibodies or rat IgG control antibodies (50 μg per mouse per day) for 2 days. **m**–**o**, Flow cytometry quantitative analysis of HSPC glucose uptake (**m**) (MFI), frequency of cycling HSPC (**n**) and apoptotic HSPC (**o**). Mean ± s.e.m., $n = 9$ mice from three independent experiments. Two-tailed Student's *t*-test; $^{**}P < 0.01$, $^{***}P < 0.005$. **p**, **q**, Frequencies of donor-derived lymphoid B220^{+} or myeloid CD11b^{+} cells in the PB of recipient mice, as were determined 24 weeks after transplantation by flow cytometry. Mean ± s.e.m., $n = 18$ donor mice from two independent experiments, for 3 recipient mice per donor. Two-tailed Student's *t*-test; $^{***}P < 0.005$. **r**–**t**, Wild-type or Endo$^{\Delta Fgfr1/2}$ mice were treated with NAC (130 mg per kg) or PBS for 7 days. Mean ± s.e.m., $n = 9$ mice from three independent experiments. Two-tailed Student's *t*-test; $^{**}P < 0.01$, $^{***}P < 0.005$. **r**, Number of circulating peripheral blood HSPC as determined by quantitative flow cytometry analysis. **s**, Number of bone marrow SLAM LSK HSPC as determined by quantitative flow cytometry analysis. **t**, Levels of chimaerism, indicating LTR-HSC contribution, were determined 24 weeks after transplantation by flow cytometry ratio analysis (CD45.2/(CD45.2 + CD45.1)). Mean ± s.e.m., $n = 24$ donor mice from two independent experiments, for 3 recipient mice per donor.

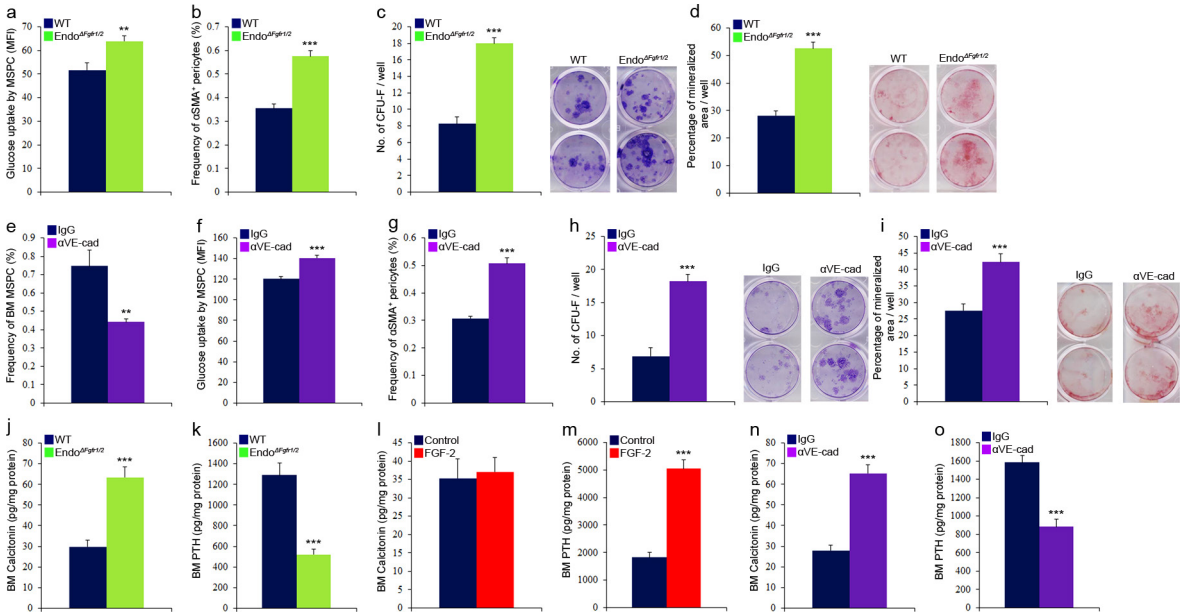

Extended Data Figure 8 | Endothelial barrier manipulation affects stromal properties, development and the levels of bone remodelling hormones. a–d, Mean ± s.e.m., $n = 9$ mice from three independent experiments. Two-tailed Student's *t*-test; $^{**}P < 0.01$, $^{***}P < 0.005$. **a**, Glucose uptake by bone marrow MSPC as determined by quantitative flow cytometry (MFI) analysis. **b**, Frequencies of bone marrow αSMA$^+$ pericytes as determined by flow cytometry analysis. **c**, Average number of scored (ImageJ) CFU-F per well and representative images. **d**, Average determined (ImageJ) percentage of mineralized area per well and representative images. **e–i**, C57BL/6 mice were treated with neutralizing rat anti-VE-cadherin antibodies or rat IgG control antibodies (50 μg per mouse per day) for 5 days. Mean ± s.e.m., $n = 9$ mice from three independent experiments. Two-tailed Student's *t*-test and one-way ANOVA with Bonferroni's multiple comparison post-hoc test; $^{**}P < 0.01$, $^{***}P < 0.005$. **e**, Frequency of bone marrow MSPC as determined by flow cytometry quantitative analysis. **f**, Glucose uptake by bone marrow MSPC as determined by quantitative flow cytometry (MFI) analysis. **g**, Frequencies of bone marrow αSMA$^+$ pericytes as determined by flow cytometry analysis. **h**, Average number of scored (ImageJ) CFU-F per well and representative images. **i**, Average determined (ImageJ) percentage of mineralized area per well and representative images. **j–o**, Bone marrow supernatants from wild-type or Endo$^{\Delta Fgfr1/2}$, PBS or FGF-2 (200 μg per kg) treated for 7 days, and IgG or rat anti-VE-cadherin (50 μg per mouse per day) for 5 days, were isolated and bone marrow concentrations of calcitonin and PTH hormones were determined using an ELISA assay. Mean ± s.e.m., $n = 9$ mice per group from three independent experiments. Two-tailed Student's *t*-test; $^{***}P < 0.005$.

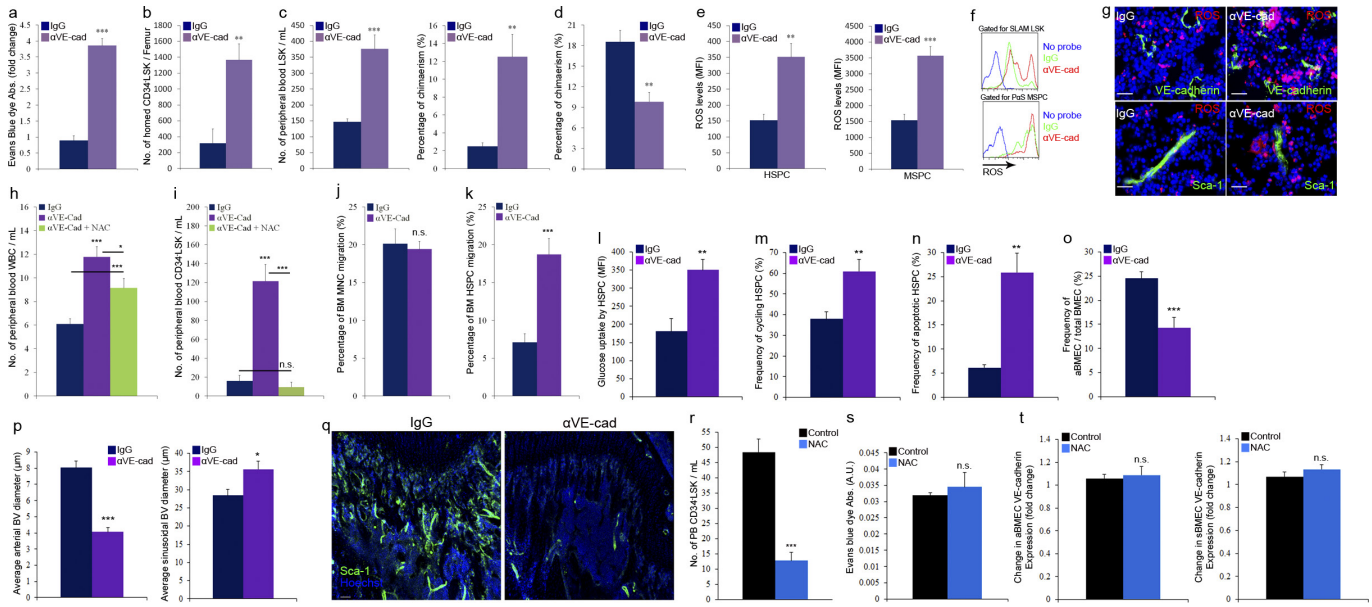

Extended Data Figure 9 | Pharmacological breaching of the endothelial barrier remodels the bone marrow vasculature and the stromal compartment while enhancing HSPCs egress in a ROS-dependent manner. a–j, C57BL/6 mice were treated with neutralizing rat anti-VE-cadherin antibodies or rat IgG control antibodies (50 μg per mouse per day) for 5 days. Mean ± s.e.m., unless otherwise indicated, $n = 9$ mice from three independent experiments. Two-tailed Student's *t*-test; $*P < 0.05$, $**P < 0.01$, $***P < 0.005$. **a**, EBD absorbance. **b**, HSPCs homing per femur. **c**, Quantitative analysis of blood LSK HSPC and chimaerism levels indicating LTR-HSC contribution. Mean ± s.e.m., $n = 10$ mice from two independent experiments. **d**, Chimaerism levels indicating LTR-HSC contribution. Mean ± s.e.m., $n = 18$ donor mice from two independent experiments, for 3 recipient mice per donor. **e**, **f**, Quantitative analysis and representative histogram plots of HSPCs and PαS MSPCs ROS MFI. **g**, Representative images of ROS^{high} (red) cells in proximity to blood vessels. Scale bar indicates 20 μm. **h–k**, C57BL/6 mice were treated with neutralizing rat anti-VE-cadherin antibodies or rat IgG control antibodies (50 μg per mouse per day) for 2 days. Where indicated, mice were also treated with NAC (130 mg per kg) or PBS for 2 days. Mean ± s.e.m., $n = 9$ mice from three independent experiments. Two-tailed Student's *t*-test and one-way ANOVA with Bonferroni's multiple comparison post-hoc test; $*P < 0.05$, $***P < 0.005$. **h**, White blood cell (WBC) numbers in the blood circulation were determined using a haematocytometer and Turk lysis of erythrocytes. **i**, Flow cytometry quantitative analysis of $CD34^-$ LSK HSPC in the blood circulation. **j–k**, Bone marrow MNC or bone marrow lineage depleted cells from treated mice were seeded on a 5 μm pore transwell and allowed to migrate for 2 h towards CXCL12 (125 ng ml^{-1}). Following migration, the frequency of migrated bone marrow MNC or $CD34^-$/LSK HSPC was determined by flow cytometry quantitative analysis. Note preferential HSPC enhanced migration after VE-cadherin neutralization. **l–p**, C57BL/6 mice were treated with neutralizing rat anti-VE-cadherin antibodies or rat IgG control antibodies (50 μg per mouse per day) for 5 days. Mean ± s.e.m., $n = 9$ mice from three independent experiments. Two-tailed Student's *t*-test; $**P < 0.01$, $***P < 0.005$. **l**, Glucose uptake levels (MFI) by HSPC as determined by flow cytometry quantitative analysis. **m–n**, Frequencies of $Ki67^+$ cycling and $AnnexinV^+$ SLAM LSK HSPC as determined by flow cytometry quantitative analysis. **o**, Frequency of Sca-1^+ aBMEC out of the total as determined by flow cytometry quantitative analysis. **p**, Diameters of distinct types of bone marrow blood vessels in the metaphysis region as determined by ImageJ software analysis of high-resolution confocal images. **q**, Confocal representative images of Sca-1^+ (green) arterial blood vessels in the metaphysis region. Note lower abundance of arterial blood vessels following 5 days of anti-VE-cadherin treatment. Scale bar indicates 200 μm. **r–t**, C57BL/6 mice were treated with NAC (130 mg per kg) or PBS for 7 days. Mean ± s.e.m., $n = 8$ mice from two independent experiments. Two-tailed Student's *t*-test; $***P < 0.005$. **r**, Flow cytometry quantitative analysis of $CD34^-$ LSK HSPC in the blood circulation. **s**, EBD absorbance following extraction from the femur was measured using spectrophotometric analysis at 620 nm and 740 nm. **t**, VE-cadherin expression levels (MFI) on distinct types of BMEC as determined by flow cytometry quantitative analysis (arterial and sinusoidal respectively).

Distinct bone marrow blood vessels differentially regulate hematopoiesis

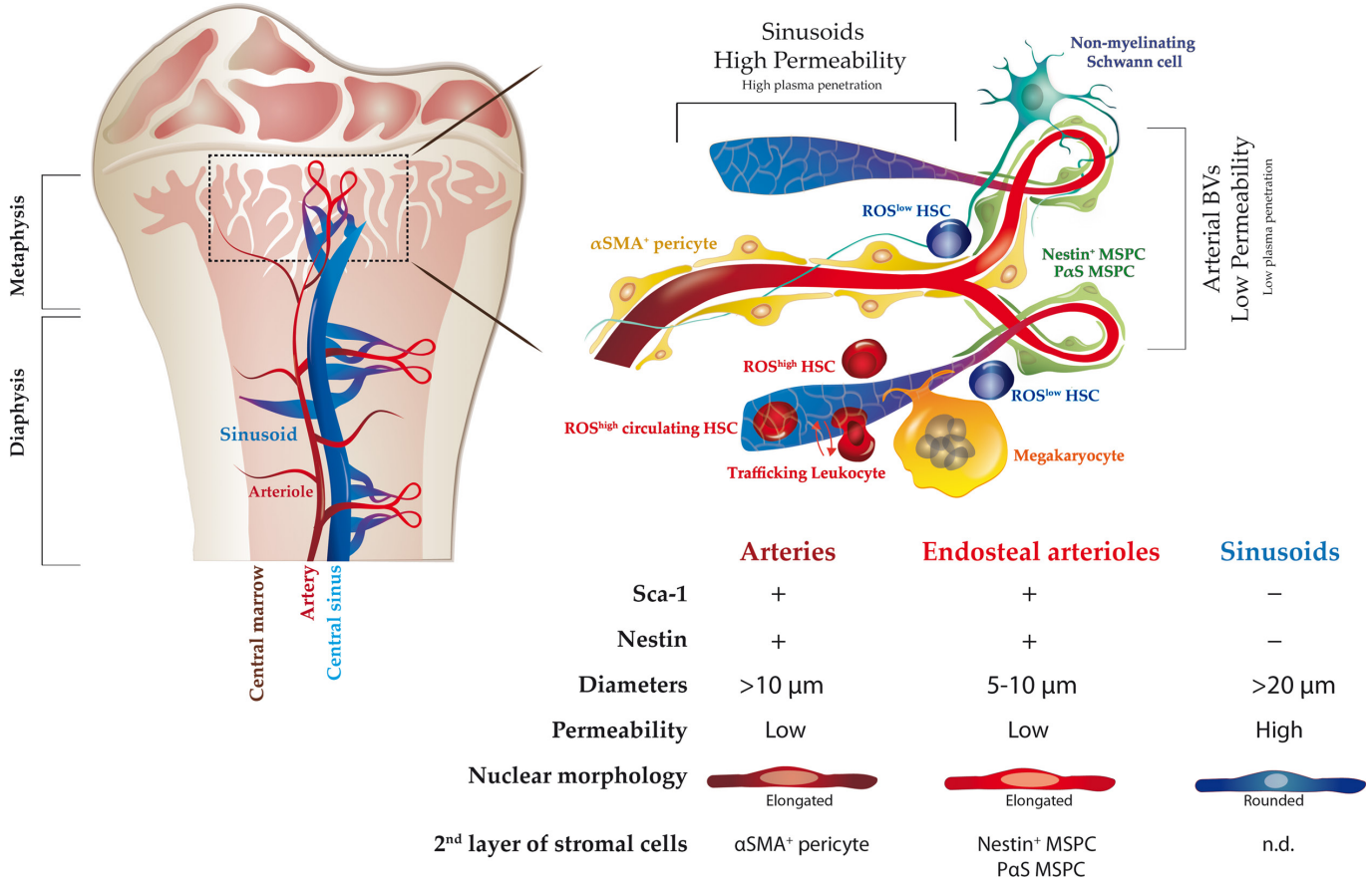

	Arteries	Endosteal arterioles	Sinusoids
Sca-1	+	+	–
Nestin	+	+	–
Diameters	>10 μm	5-10 μm	>20 μm
Permeability	Low	Low	High
Nuclear morphology	Elongated	Elongated	Rounded
2nd layer of stromal cells	αSMA+ pericyte	Nestin+ MSPC PαS MSPC	n.d.

Extended Data Figure 10 | Illustration of proposed bone marrow blood vessels model and regulation of haematopoiesis. Bone marrow vasculature is composed of two main types of blood vessels which are arterial blood vessels and sinusoids. Blood enters the bone marrow via the arteries, branching to smaller arterioles, which in proximity to endosteal areas, further branch into small-diameter endosteal arterioles. These endosteal arterioles reconnect to downstream sinusoids which drain the blood into the central sinus and out of the bone marrow. Arterial BMEC have elongated nuclear morphology, express Sca-1 and nestin markers, and display high barrier integrity properties. In addition, arterial blood vessels display the highest blood flow speed and shear rate. Arterial BMEC maintain a microenvironment that promotes low ROS state of HSCs in its surrounding. The second layer of cells associated with arteries is composed of αSMA^{+} pericytes, while endosteal arterioles are associated with HSC-supportive MSPCs. The association of MSPCs and ROS^{low} HSCs with endosteal capillaries suggests the existence of an osteo-vascular niche where the residing HSCs are influenced by both endosteal and vascular elements simultaneously. Innervating Schwann cell nerve fibres, shown to maintain HSC dormancy, were found to be associated with arteries and endosteal arterioles. More permeable fenestrated sinusoids induce higher ROS state in their surroundings, and have slower internal blood flow, all of which makes them the ultimate candidate to serve as the site for bone marrow cellular trafficking. Megakaryocytes found in sinusoidal sites support and maintain HSPC in a ROS low state. Live real-time imaging indicates that all leukocyte trafficking occurs exclusively via sinusoids. Furthermore, experimental systems manipulating endothelial barrier integrity provide evidence that more fenestrated endothelial state promotes trafficking at the expense of stem cell maintenance. Yet, conditions enhancing endothelial integrity, reducing cellular trafficking promote bone marrow stem cell expansion and maintenance. Peripheral blood plasma, which can penetrate into the bone marrow more easily via fenestrated blood vessels, enhances HSPC migratory capacity but hampers their long-term repopulation capacity and survival. Thus, the state of the endothelial blood–bone-marrow barrier in distinct blood vessels and under steady state or 'stress' conditions may have a strong regulatory impact on tissue residing stem cells.

CORRIGENDUM

doi:10.1038/nature19088

Corrigendum: Distinct bone marrow blood vessels differentially regulate haematopoiesis

Tomer Itkin, Shiri Gur-Cohen, Joel A. Spencer, Amir Schajnovitz, Saravana K. Ramasamy, Anjali P. Kusumbe, Guy Ledergor, Yookyung Jung, Idan Milo, Michael G. Poulos, Alexander Kalinkovich, Aya Ludin, Karin Golan, Eman Khatib, Anju Kumari, Orit Kollet, Guy Shakhar, Jason M. Butler, Shahin Rafii, Ralf H. Adams, David T. Scadden, Charles P. Lin & Tsvee Lapidot

Nature **532,** 323–328 (2016); doi:10.1038/nature17624

The authors Karin Golan, Eman Khatib and Anju Kumari were erroneously omitted from the author list of this Article. They are all associated with the affiliation: Department of Immunology, The Weizmann Institute of Science, Rehovot 76100, Israel, and the Author Contributions section should have included the following statements: K.G. participated in CFU-F and CFU-Ob related experiments; E.K. participated in metabolic ROS experiments, including plasma penetration and NAC treatment; A.K. participated in mice genotyping.

In addition, during preparation of the final figures, the colours of the curves in Fig. 2b were erroneously switched. The top curve should be in blue indicating sinusoids with higher leakage, and the bottom curve should be in red indicating arterioles with lower leakage. These errors have all been corrected online.